
Unterschrift Betreuer



TECHNISCHE
UNIVERSITÄT
WIEN

Vienna University of Technology

DIPLOMARBEIT

The Hematite (012) Surface: Structure and Reactivity

ausgeführt am Institut für Angewandte Physik
der Technischen Universität Wien

unter der Anleitung von
Gareth Parkinson

durch

Florian Kraushofer

Pappenheimgasse 35/1.1, 1200 Wien

22. März 2017

Unterschrift Student

Kurzfassung

Eisenoxide gehören zu den häufigsten Materialien der Erdkruste und weisen Eigenschaften auf, die Relevanz für eine Vielfalt von Anwendungen haben, unter anderem für Katalyse, Biomedizin und Magnetismus. Das stabilste Eisenoxid unter Atmosphärenbedingungen ist Hämatit ($\alpha\text{-Fe}_2\text{O}_3$), das wegen seiner Stabilität in Wasser, ökologischen Verträglichkeit und 1.9-2.2 eV Bandlücke als vielversprechendes Material für die photoelektrochemische (PEC) 'water splitting'-Reaktion einige Aufmerksamkeit erhalten hat. Theoretisch könnte mit Hämatit eine maximale Solar-zu-Wasserstoff-Effizienz von 15% erreicht werden, was für praktische Anwendungen ausreichen würde. Die tatsächliche Leistungsfähigkeit wird allerdings durch einen niedrigen Absorptionskoeffizienten, kurze Minoritätsträger-Lebenszeit, niedrige Leitfähigkeit und schwerfällige Reaktionskinetik behindert. Dazu kommt, dass die stabilste Hämatit-Oberfläche, die (012)-Ebene, auf atomarer Ebene nur unzureichend verstanden ist.

In dieser Arbeit wurden die zwei Terminierungen der $\alpha\text{-Fe}_2\text{O}_3(012)$ -Oberfläche und deren Reaktivität mittels Rastertunnelmikroskopie (STM), Röntgenphotoelektronenspektroskopie (XPS), Ultraviolettphotoelektronenspektroskopie (UPS), Augerelektronenspektroskopie (AES), Beugung niederenergetischer Elektronen (LEED) und Temperatur-programmierter Desorption (TPD) untersucht. Die Ergebnisse unterstützen die bisherige Annahme einer 'bulk termination' der oxidierten Oberfläche, aber keines der bisher vorgeschlagenen Modelle für die (2×1) -Oberflächenrekonstruktion unter reduzierenden Bedingungen scheint korrekt zu sein. Ein neues Modell für die (2×1) -Terminierung wird daher vorgeschlagen.

Die Reaktivität der Oberflächen mit Wasser entspricht zuvor publizierten Ergebnissen in dem Aspekt, dass Wasser auf beiden Terminierungen teilweise dissoziiert. Zwei klar ausgeprägte Phasen der Anordnung von Hydroxylen, abhängig von der Bedeckung, wurden mit STM auf der (2×1) -Rekonstruktion beobachtet und anschließend mittels LEED, TPD und XPS analysiert.

Vorläufige Daten zu Sauerstoff-Adsorption, den Effekten von atomarem Wasserstoff, sowie der Oberflächeninteraktion mit Titan- und Platin-Adatomen werden vorgestellt. Das bisherige Verständnis von Sauerstoff-Adsorption wird im Temperaturregime unter 100 K erweitert. Physisorption von O_2 bei niedrigen Temperaturen scheint eine Voraussetzung für eine Transformation der (2×1) -Oberfläche zu sein.

Abstract

Iron oxides are among the most common materials in Earth's crust, and exhibit properties relevant to a wide range of applications including catalysis, biomedicine, and magnetism. The most stable iron oxide under atmospheric conditions is hematite ($\alpha\text{-Fe}_2\text{O}_3$), which has received much attention as a promising material for photoelectrochemical (PEC) water splitting due to its stability in water, ecological agreeability and 1.9-2.2 eV bandgap. In theory, hematite can achieve a maximum solar-to-hydrogen efficiency of 15%, sufficient for practical application. However, its actual performance is hindered by a low absorption coefficient, short minority carrier lifetime, low conductivity and sluggish reaction kinetics. Furthermore, the most stable $\alpha\text{-Fe}_2\text{O}_3$ surface, the (012) facet, is poorly understood at an atomic scale.

In this thesis, the two terminations of the $\alpha\text{-Fe}_2\text{O}_3$ (012) surface and their reactivity were investigated by scanning tunnelling microscopy (STM), low energy electron diffraction (LEED), x-ray photoelectron spectroscopy (XPS), ultraviolet photoelectron spectroscopy (UPS), Auger electron spectroscopy (AES) and temperature programmed desorption (TPD). The data support the previously assumed bulk termination model for the oxidized surface, but none of the models proposed for the (2×1) surface reconstruction under reducing conditions appear to be correct. A new model for the (2×1) termination is therefore proposed.

Reactivity of the surfaces to water fit previously published results in that H_2O is found to partly dissociate on both surface terminations. Two distinct phases of hydroxyl ordering, depending on coverage, are found on the (2×1) reconstruction with STM and subsequently analysed with LEED, TPD and XPS.

Preliminary data on oxygen adsorption, the effects of atomic hydrogen, as well as surface interaction with titanium and platinum adatoms is presented. The previous understanding of O_2 adsorption on the surface is expanded in the temperature regime below 100 K. Low temperature physisorption of O_2 is found to be a precondition for a transformation of the (2×1) surface.

Contents

1	Experimental Methods	8
1.1	Low Energy Electron Diffraction (LEED)	8
1.2	X-Ray Photoelectron Spectroscopy (XPS)	8
1.3	Ultraviolet Photoelectron Spectroscopy (UPS)	8
1.4	Auger Electron Spectroscopy (AES)	9
1.5	Temperature Programmed Desorption (TPD)	9
1.6	Scanning Tunneling Microscopy (STM)	9
2	Experimental Setup	11
2.1	Ultra-high vacuum chambers	11
2.1.1	Room-temperature STM chamber (RT)	11
2.1.2	Omega chamber	11
2.1.3	Machine for Reactivity Studies (MRS)	11
2.2	The samples	11
3	Introduction	13
3.1	The α -Fe ₂ O ₃ (012) surface	14
4	Results	16
4.1	Preparation	16
4.2	The clean surfaces	17
4.3	Surface interaction with gaseous water	24
4.4	Surface interaction with liquid water	36
4.5	O ₂ adsorption	37
4.6	Effects of molecular and atomic hydrogen	37
4.7	Ti adatoms	40
4.8	Other results	41
5	Discussion	45
5.1	The clean surfaces	45
5.2	Surface interaction with water	48
5.3	Preliminary data	52
6	Summary and Outlook	54

1 Experimental Methods

1.1 Low Energy Electron Diffraction (LEED)

Low Energy Electron Diffraction is widely used to determine symmetries at a sample surface by observing the diffraction pattern of a collimated beam of electrons. The energy of the electrons typically lies between 20-500 eV, which corresponds to a De Broglie wavelength of 0.5-2.7 Å, which is in the order of magnitude of inter-atomic distances in most solids. The low mean free path of the electrons inside the solid, which at these energies is in the order of 5-10 Å, results in high surface sensitivity.

Scattered electrons interfere constructively at any point in space where the Laue relation is fulfilled, which in reciprocal space is $k - k_0 = G_{hkl}$, with the wave vector of the incident electron k_0 , the wave vector of the diffracted electron k and any vector of the reciprocal lattice G_{hkl} . For surface diffraction, two-dimensional scattering is simply given by $k^{\parallel} - k_0^{\parallel} = G_{hk}$, where G_{hk} is a vector in the two-dimensional reciprocal lattice of the surface, and k^{\parallel} and k_0^{\parallel} are the components parallel to the sample surface of the aforementioned wave vectors. This two-dimensional condition yields lines perpendicular to the sample surface instead of points, as the three-dimensional Laue condition would. By placing a hemispherical screen in front of the sample, these lines are finally resolved as a point pattern corresponding to the surface crystal structure in reciprocal space. Since the length of the wave vector depends on the electron energy, higher energies yield more points on the screen, since more G_{hk} vectors fulfil the Laue condition. The same is true if surface periodicity is increased, since a larger lattice vector in real space corresponds to a smaller one in reciprocal space. Thus, a reconstruction of a (1×1) surface to a (2×1) termination, for example, leads to twice as many points observed per screen area at the same electron beam energy.

1.2 X-Ray Photoelectron Spectroscopy (XPS)

The general principle of Photoelectron Spectroscopy is to irradiate a solid with photons, which results in the emission of electrons due to the photoelectric effect. By measuring the energy of these electrons and comparing to the energy of the incident photons, their original binding energy can be determined, yielding information about the elemental composition and chemical bonding states of the sample. For X-Ray Photoelectron Spectroscopy, either an Al or a Mg anode is generally applied, which emit photons with characteristic energies of ≈ 1486 eV or 1253 eV, respectively. Although these photons penetrate several μm of the sample, XPS is highly surface sensitive due to the low inelastic mean free path of the emitted electrons while they are still in the sample. However, spatial resolution depends on how well the x-ray beam can be focussed, as well as on the acceptance characteristics of the analyser, and is usually low. Additional information can be obtained by measuring both emission perpendicular to the sample and emission at a higher angle. Since the surface sensitivity of XPS is limited by the mean free path of the emitted electrons in the solid and a higher emission angle results in a longer distance electrons have to cover, the differences between bulk and surface states will be highlighted when comparing normal and grazing exit measurements.

1.3 Ultraviolet Photoelectron Spectroscopy (UPS)

Ultraviolet Photoelectron Spectroscopy is functionally identical to XPS, but is limited to states near the Fermi edge due to the lower photon energy. However, much higher energy resolution

can be achieved in that energy regime, allowing analysis of the fine structure in the valence region. This is especially useful when studying adsorbed molecules, since UPS can be used to study their bonding states. Additionally, the work function of a surface can be measured by UPS by comparing to the energy of the incident photons to the low kinetic energy cutoff of the photoelectrons.

1.4 Auger Electron Spectroscopy (AES)

Auger Electron Spectroscopy utilizes the Auger effect, which is an alternative relaxation process of excited atoms occurring in competition with simple x-ray emission. When core electrons are removed from sample atoms by bombarding with high energy electrons in the range of several eV to 50 keV, there are multiple possibilities as to which electrons can transition into the resulting core holes. If an electron from an outer shell fills such a core hole, the transition energy can be higher than the binding energy of another outer shell electron, in which case that electron can be emitted. Its kinetic energy will then depend on the energy of all three involved states. As with XPS, the high surface sensitivity of AES is given by the low inelastic mean free path of the emitted electrons on their way to the surface. However, quantitative analysis of the results is much more difficult due to the comparatively high complexity of the process.

1.5 Temperature Programmed Desorption (TPD)

For Temperature Programmed Desorption, some gaseous molecule species of interest is first adsorbed on a surface at a low temperature. The interaction of the molecules with the surface is then studied by heating at a constant rate, usually between 1 and 10 K/s. The desorbing molecules are then analysed by a mass spectrometer, yielding a separate curve for each desorbed species, which might not be identical to the originally adsorbed gas. Since the binding energies of adsorbed molecules can depend strongly on neighbouring adsorbates, additional information about the surface reactivity can be obtained by measuring with different starting coverages and studying the shifts in onsets and maxima of the desorption peaks.

1.6 Scanning Tunneling Microscopy (STM)

Scanning Tunneling Microscopy is based on the quantum-mechanical tunnel effect, due to which particles can, with a small probability, 'tunnel' through potential barriers where they would classically be reflected. In STM, a conductive tip, which ideally ends in a single atom, is brought close to a conductive sample, and a bias is applied. The resulting tunnelling current is a function of bias, tip-sample distance, and the local density of states in the sample. Keeping either the current constant by varying the z position of the tip, or vice versa, scanning over the x and y directions ideally results in atomic resolution images of either filled or empty states near the Fermi level. Typical values for bias, tunnelling current and distance from the sample are $U = \pm 1 \text{ mV} - 5 \text{ V}$, $I = 0.01 - 10 \text{ nA}$ and $d = 0.5 \text{ nm}$.

The tunnelling current is given by $I \propto e^{-2\kappa d}$, where κ is the decay length $\kappa^2 = 2m(V_B - E)/\hbar^2$. V_B can be considered the height of a potential barrier between electron states of the tip and of the sample. Due to the exponential dependence of the tunnelling current on the tip-sample distance, even small changes in the z position result in a strong feedback current and can be corrected.

When a positive bias is applied to the sample, electrons tunnel from filled states of the tip to empty states of the sample. Potentially, all empty states in the sample below the Fermi level of

the tip shifted upwards by the applied bias are available for tunnelling into. Conversely, when a negative bias is applied to the sample, tunnelling occurs from filled electron states of the sample to empty states of the tip. Again, all filled states of the sample above the downwards shifted Fermi level of the tip contribute to the tunnelling current, with the sample states near the Fermi level contributing most.

Since the tunnelling current depends not only on the distance but also on the density of states of the sample, tip positions where the highest tunnelling current is measured do not necessarily correspond to the atoms sticking out most from the sample. Atoms of a different species with a higher density of states might contribute more to the tunnelling current, even if they are farther away from the surface. Therefore, STM images are often hard to interpret, especially if the density of states of the sample is unknown.

2 Experimental Setup

All experiments were performed on single crystals using the techniques mentioned above in ultra-high vacuum (UHV) systems, which will be described here. Where the same technique was available in different chambers, results were successfully reproduced, thus ensuring their consistency even when preparation parameters varied slightly due to different chamber setups.

2.1 Ultra-high vacuum chambers

2.1.1 Room-temperature STM chamber (RT)

The RT vacuum system consists of a a preparation chamber and a main chamber for measurements. The main chamber is equipped with an Omicron μ STM, a LEED module (VSI), a quadrupole mass spectrometer (Balzers), an AES module (Perkin-Elmer) and an XPS module (SPECS). The preparation chamber houses a sputter source, an electron gun for heating the sample holder and a quadrupole mass spectrometer (Hiden), as well as leak valves that allow dosing Ar, O₂ and H₂O. Typical pressures in the main chamber and the preparation chamber are below $0.8 \cdot 10^{-10}$ mbar and below $1.0 \cdot 10^{-10}$ mbar, respectively.

2.1.2 Omega chamber

The Omega chamber is a compact system with a base pressure $< 10^{-10}$ mbar, equipped with a commercial LEED setup (Omicron), a quadrupole mass spectrometer (SRS), an Omicron STM 1 and a SPECS dual anode x-ray source together with a SPECS Phoibos HSA 3500 analyzer. All preparation, including sputtering, heating and dosing O₂ and Ar, happens in the main chamber. The main asset of the system is a glassware compartment that can be attached to the loadlock, allowing clean transfer of samples to an environment where liquid water can be applied to the surface, and back to UHV.

2.1.3 Machine for Reactivity Studies (MRS)

The machine for reactivity studies is a chamber with base pressure $5 \cdot 10^{-11}$ mbar, combining a SPECS Phoibos 150 energy analyser, a SPECS FOCUS 500 monochromated x-ray source (Al K or Ag L anode), a SPECS UVS10/35 source with both He I and He II discharge, and a commercial LEED setup with a custom-built molecular beam source and a HIDEN HAL 3F PIC quadrupole mass spectrometer (QMS) for TPD measurements. The sample holder is fixed to a helium flow cryostat, allowing access to a wide temperature range from ≈ 40 to 1200 K. The molecular beam allows precision dosing of gasses to a defined beam spot on the sample, so adsorption on other surfaces can be avoided during TPD measurements.

2.2 The samples

Four different samples were used in total, two of them acquired from SurfaceNet GmbH, and two from SPL, all with a nominal precision of $\pm 0.1^\circ$. After initial cleaning cycles sputtering with 1 kV Ar⁺ ions and annealing in UHV, all contaminants detectable by XPS were successfully removed from the four samples, save for a small K peak on one of the crystals. However, all samples initially exhibited strong charging in LEED at room temperature below electron energies of about 90 eV. STM was therefore not attempted before the conductivity had been increased to a level where no charging was observed in LEED above 20 eV electron energy,

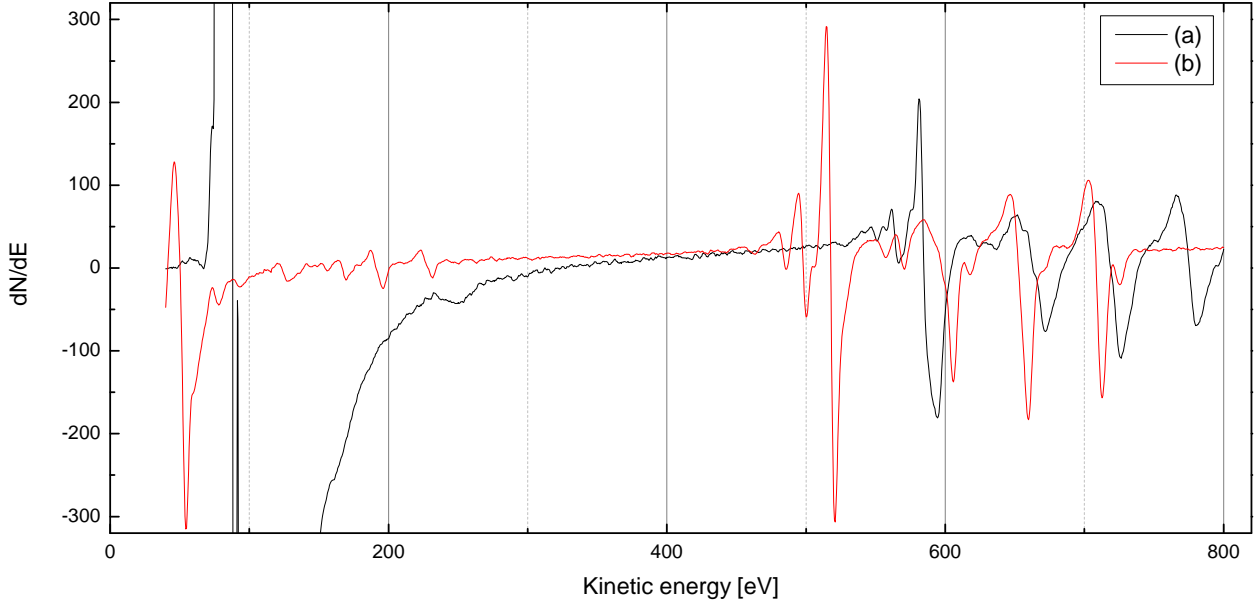


Figure 1: AES spectra of one of the samples (a) after 47 sputtering/annealing cycles and (b) after 95 sputtering/annealing cycles. Mo peaks at low energies in (b) are attributed to the Mo sample holder. The peak shift was ≈ 70 eV towards higher kinetic energy in (a), presumably due to charging, and could be reduced to ≈ 7 eV in (b).

which was achieved by 60-100 cycles of sputtering with 1 kV Ar^+ or He^+ ions and annealing in UHV ($T = 630^\circ\text{C}$). During this preparation process, the samples were also annealed in oxygen ($p_{\text{O}_2} = 1 \cdot 10^{-6}$ mbar, $T = 550^\circ\text{C}$) every 5-10 cycles to prevent the surface from being reduced to Fe_3O_4 . The improvement in conductivity can be qualitatively measured via the peak shift in AES, as shown in Fig. 1.

Unfortunately, two of the samples were at some point apparently heated too high in UHV, yielding unexpected reconstructions on part of the surface area. One of these two samples (#392) subsequently exhibited a (3×1) LEED pattern superimposed on (2×1) on about half of the crystal area, both in an oxidized and in a reduced state, probably due to a partial reconstruction to Fe_3O_4 . The other sample (#394) behaved completely normal when reduced, but reconstructed to a peculiar (2×3) structure along the edges when oxidized. Since this was the crystal with the K contamination mentioned above, no conclusion can be reached with any certainty on whether doping, preparation temperature or some other unknown quality of the sample caused this unexpected behaviour.

Both samples were subsequently only used for STM experiments limited to the crystal area that exhibited the standard LEED patterns. All other measurements were conducted on the two samples with homogeneous surface behaviour to avoid contributions from the unknown phases.

3 Introduction

Iron oxides are a class of materials used for a wide range of applications, among other things in catalysis, corrosion, and magnetism. Studying them is also promising due to their abundance in nature, since iron and oxygen are among the four most common elements in the Earth's crust. At atmospheric conditions, the most stable iron oxide is hematite (α -Fe₂O₃), easily recognizable in nature due to its distinctive red colour. Hematite is non-toxic, stable and has a 1.9-2.2 eV bandgap [1], which makes it a promising material as an anode in photoelectrochemical water splitting. Conceptually, such cells work by having electromagnetic radiation, such as sunlight, generate electron-hole pairs in a photoanode. The electrons are then transferred to a cathode where they reduce water to H₂ and OH⁻, while the holes are used for OH⁻ oxidation to O₂ at the anode, thus generating spatially separated H₂ and O₂ gas.

In theory, hematite can achieve a maximum solar-to-hydrogen efficiency of 15% [2], which would be comfortably above the benchmark efficiency of 10% required for practical applications. However, there are several challenges remaining, reducing the practical efficiency. While the bandgap of hematite is well suited to use the bulk of solar radiation, its absorption coefficient is low [3], so a lot of material is required to utilize all of the incident radiation. At the same time, however, minority carrier exhibit only a short lifetime [4], conductivity is low [5, 6], and hematite exhibits poor surface kinetics [7, 8]. While some progress has been made in improving the performance of hematite as a photoanode by approaches such as oxygen vacancies engineering [9] or titanium doping [10, 11], a fundamental understanding of surface structure and chemistry would allow a more systematic approach.

A large body of work already exists for the α -Fe₂O₃(001) surface, also known as the C-cut surface. Its exact termination is still disputed, and several different phases have been observed depending on preparation [12–16]. However, since the conductivity of Fe₂O₃ is anisotropic [17, 18] and lowest in the [001] direction, STM measurements of stoichiometric (001) surfaces are mostly done on thin films grown on conductive substrates, and (001) terminated single crystals are difficult to work with [12–14]. An additional problem not limited to the (001) surface is that when studying oxidation and reduction of Fe₂O₃, the preparation frequently requires conditions close to the phase boundary between Fe₂O₃ and Fe₃O₄ [19, 20], and re-oxidation of magnetite may require high oxygen pressures not available in most typical UHV systems.

In comparison, there are relatively few publications to date on the α -Fe₂O₃-(012) surface [21–31], even though it is the most stable α -Fe₂O₃ termination according to density functional theory (DFT) calculations [32], and prevalent in nano-hematite [14, 33]. While the existence of both a (1×1) and a (2×1) termination of the (012) surface, prepared by annealing in O₂ or ultra-high vacuum (UHV), respectively, have been shown repeatedly [21–23], no conclusive evidence as to its atomic-scale structure has been published.

A schematic image of the orientation of the α -Fe₂O₃(012) surface relative to the crystal lattice is shown in Fig. 2 (a). The (012) surface is also often denoted as the R-cut surface, and the three-digit notation (012) is equivalent to ($\bar{1}$ 02) and (1 $\bar{1}$ 2), as well as to (01 $\bar{1}$ 2), ($\bar{1}$ 012) and (1 $\bar{1}$ 02) in the four-digit nomenclature.

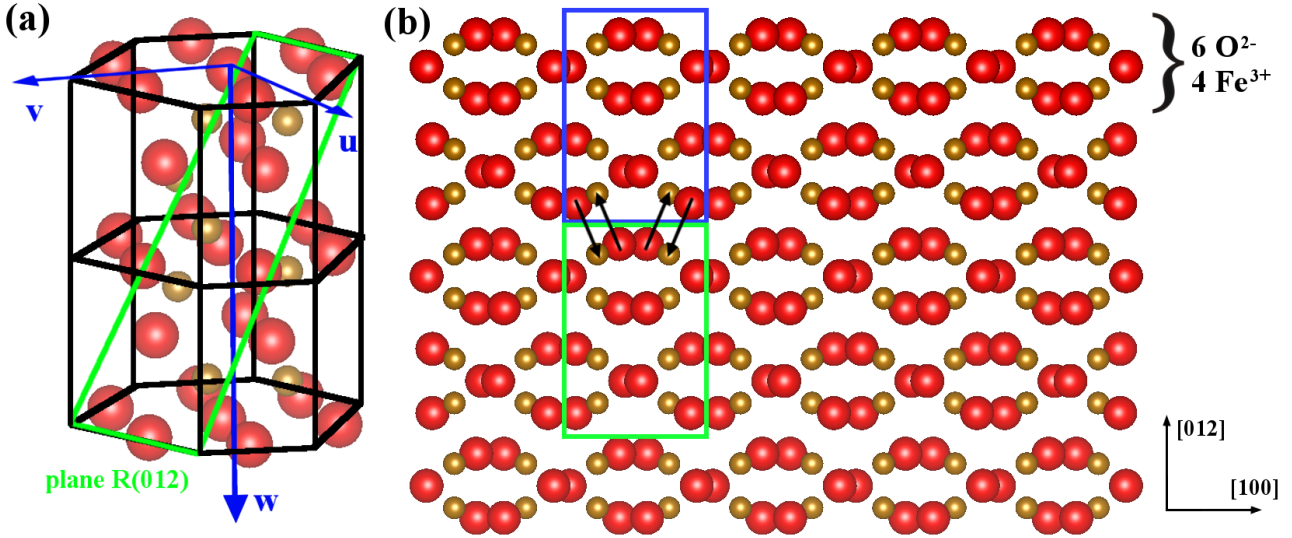


Figure 2: (a) Schematic image of the R-cut. (b) Side view of the bulk-terminated R-cut surface with repeat units highlighted; red: oxygen, golden: iron

3.1 The $\alpha\text{-Fe}_2\text{O}_3(012)$ surface

The first results on the (012) surfaces structure were presented by Lad and Heinrich in 1988 [21], who report observing a (2×1) reconstruction in LEED when annealing at low O_2 partial pressures. Gautier-Soyer et al. revisited the subject in 1995 [22], and based on LEED and AES proposed a reconstruction model extending 25-30 Å into the bulk. However, when Henderson et al. conducted high resolution electron energy loss spectroscopy (HREELS) studies in 1998 [23], they concluded that based on optical phonon modes, the (2×1) reconstruction was likely restricted to the immediate surface layer. Henderson proceeded to accumulate data on the (2×1) surface based on TPD, HREELS, LEED and static secondary ion mass spectrometry (SSIMS) [23–25, 31].

All publications agree that the (1×1) termination is most probably a simple bulk-terminated surface. A schematic side view of the unrelaxed bulk termination is shown in Fig. 2 (b). The repeat unit in the [012] direction is highlighted by the blue and green rectangles. Each rectangle contains 12 O^{2-} and 8 Fe^{3+} ions, resulting in a Tasker type 2 surface [34] with no dipole moment perpendicular to the surface, which means that the (1×1) bulk terminated surface can conceptually be stable. A cut along the interface of the green and blue rectangles breaks as many oxygen \rightarrow iron bonds as iron \rightarrow oxygen bonds, as indicated by the black arrows, which again indicates an auto-compensated surface.

It is worth noting that the first and third layer of oxygen (pink and dark red in Fig. 3 (b)) are not equivalent to the second layer (red in Fig. 3 (b)). While the number of oxygen atoms per unit cell and the distance between oxygen atoms in the $[12\bar{1}]$ direction is the same, the atoms in the second layer of oxygen are packed more closely in the [100] direction. However, the top and bottom half of the repeat units marked in Fig. 2 (b) are equivalent and only shifted by half a unit cell in the [100] direction.

Each iron atom is coordinated with two oxygen atoms directly above it and two oxygen atoms directly below it, as well as with one oxygen atom two layers above it and one two layers below it, as shown in Fig. 3 (a). In a bulk-terminated configuration, the iron atoms at the surface therefore have one less bond than the ones in the bulk, as have the topmost oxygen atoms.

For the (2×1) reconstruction, Henderson proposes a simple oxygen vacancy model, with every

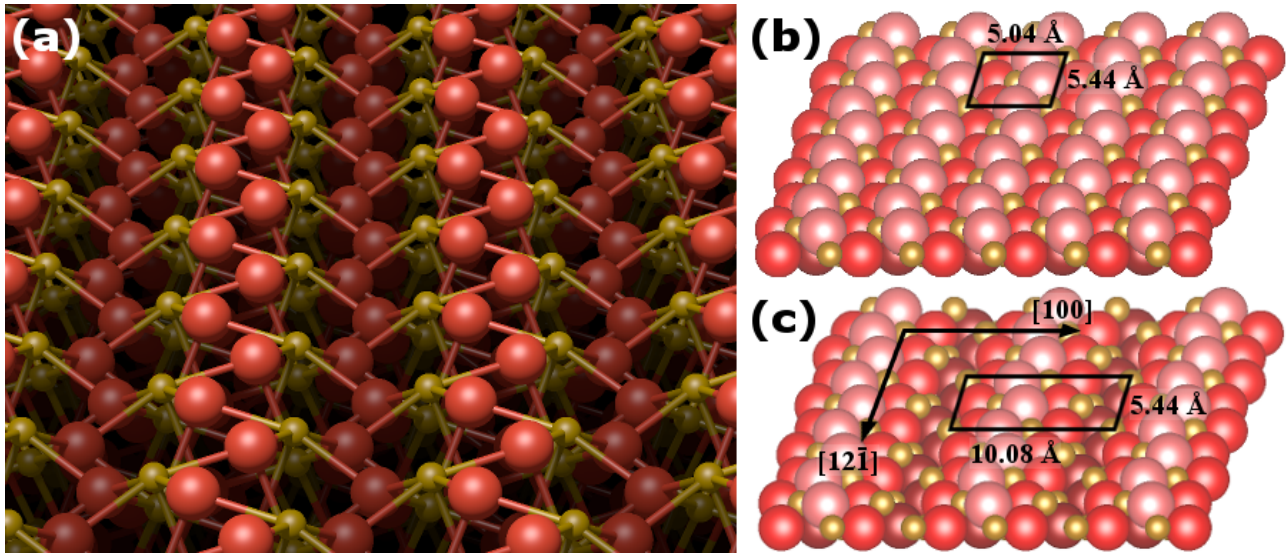


Figure 3: Schematic model of the unrelaxed bulk terminated (012) surface (a, b) and the previously suggested (2×1) reconstruction (c) [23], in which every other oxygen row is removed. Fe atoms are golden, O atoms are pink, red and dark red.

other topmost oxygen row missing entirely [23], as shown in Fig. 3 (c). However, even though Henderson cautions that significant relaxations are to be expected for his model, no DFT examination to determine its relaxed structure and stability were ever attempted, and no scanning probe data have been published to date to support or refute either of the proposed models. Whatever their configuration, both $\alpha\text{-Fe}_2\text{O}_3(012)$ terminations have been shown to dissociate water by Henderson et al. [23], warranting further investigation of water adsorption and reactivity.

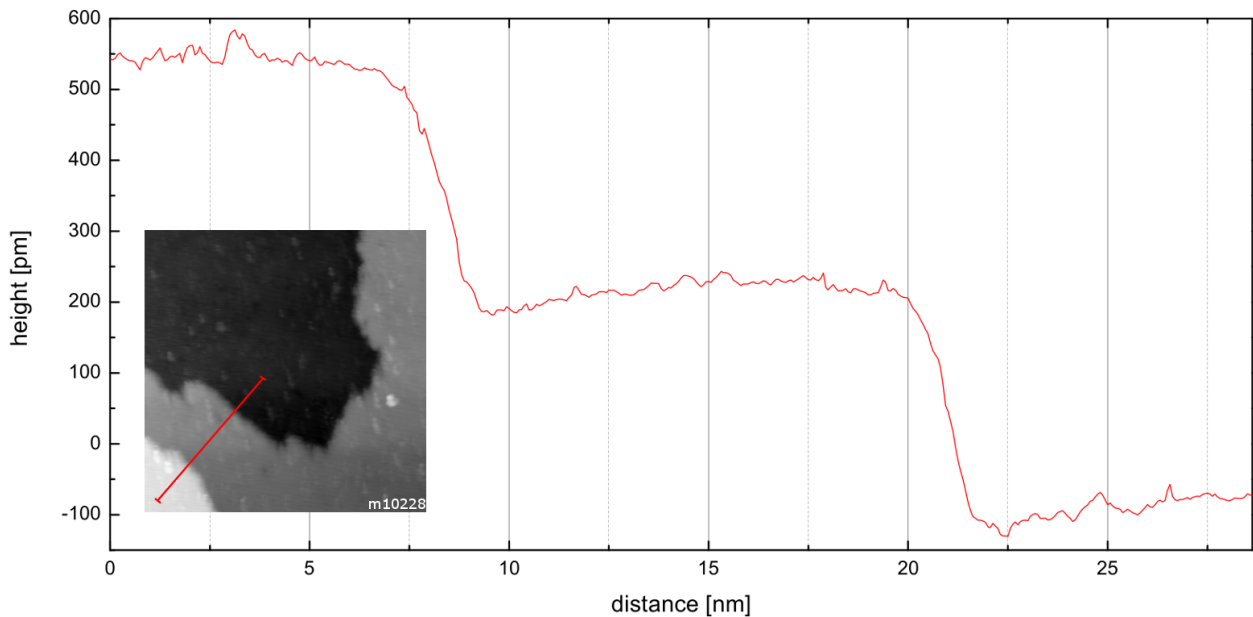


Figure 4: Height profile along the red line in the STM image of the (1×1) surface shown in the inset ($50 \times 50 \text{ nm}^2$, $U = +3 \text{ V}$, $I = 0.1 \text{ nA}$). The step height is measured to be $\approx 3.7 \text{ \AA}$, which is the expected value and corresponds to half the repeat unit in the $[012]$ direction marked in blue in Fig. 3 (b).

4 Results

4.1 Preparation

After initial cleaning and reduction of the samples, as described in chapter 2.2, the (2×1) reconstruction could be prepared either after sputtering or directly from the (1×1) surface by annealing in UHV ($T = 630^\circ\text{C}$). In the same way, the (1×1) surface could be prepared from a freshly sputtered crystal or from the (2×1) termination by annealing in oxygen ($p_{\text{O}_2} = 1 \cdot 10^{-6} \text{ mbar}$, $T = 550^\circ\text{C}$). The surfaces were kept clean by occasional sputtering with 1 kV Ar^+ or He^+ ions (RT chamber: $p_{\text{Ar}} = 8 \cdot 10^{-6} \text{ mbar}$, $I = 1.8\text{-}1.9 \mu\text{A}$; Omega chamber: $p_{\text{Ar}} = 1 \cdot 10^{-6} \text{ mbar}$, $I = 0.4\text{-}0.5 \mu\text{A}$; MRS: $p_{\text{He}} = 1.5 \cdot 10^{-5} \text{ mbar}$, $I = 1.3\text{-}1.4 \mu\text{A}$; disparities due to lower sputter gun capabilities were compensated by longer sputtering times).

It should be mentioned that only in the MRS (see chapter 2.1.3) was the thermocouple for temperature measurements attached directly to the sample holder and calibrated with a pyrometer, yielding the accuracy required for TPD measurements. In all other chambers, temperature readings were taken at the sample manipulators and are therefore not directly related to the samples' surface temperatures. Pyrometer readings revealed that samples were systematically cooler than the temperature readout by values on the order of magnitude of 50°C , and preparation temperatures were slightly adapted for each sample so as to get the best results, which were evaluated using LEED. Preparation temperature given in this thesis usually refer to the temperate readout of the thermocouples, so a systematic error should be kept in mind.

Although large terraces were relatively easy to find on both the (1×1) and the (2×1) surface after annealing, the total amount of steps as imaged by STM remained high on all samples. A typical height profile is shown in Fig. 4. Steps on either surface are found to have a height of $\approx 3.7 \text{ \AA}$, or multiples thereof, which corresponds to half a repeat unit in the $[012]$ direction. Since this is the periodicity of planes in which a non-polar cut can be made, it is not surprising

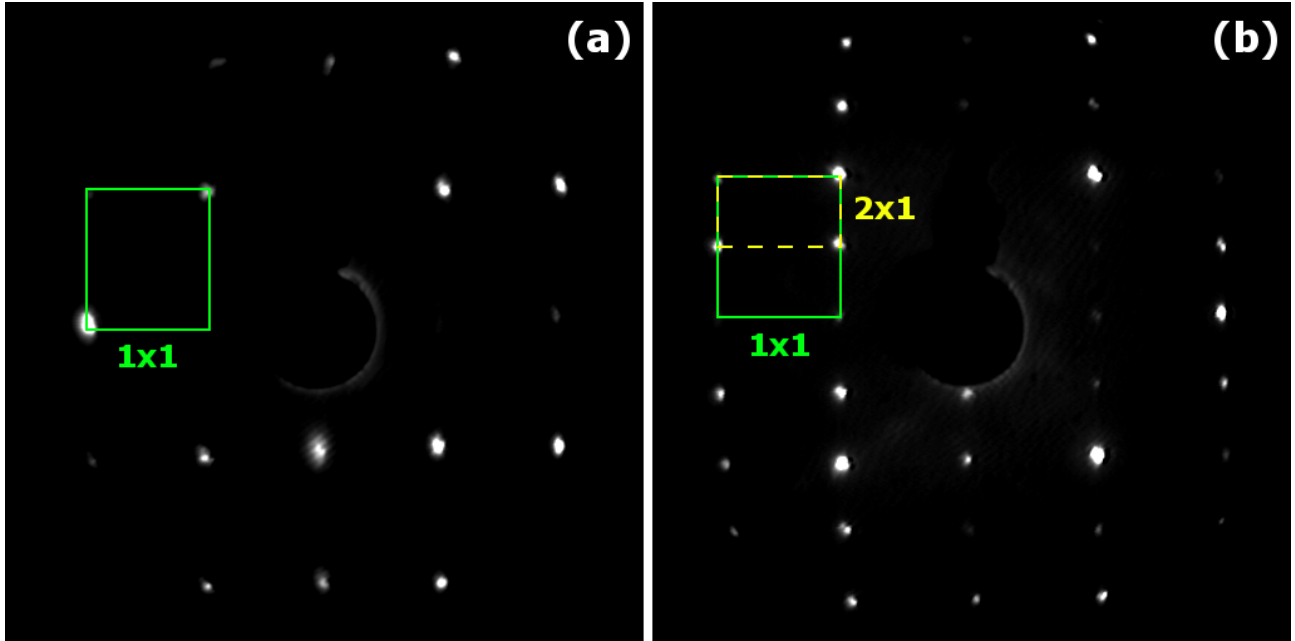


Figure 5: LEED patterns of the clean (1×1) (a) and (2×1) (b) α -Fe₂O₃(012) surfaces. Electron beam energy = 50 eV

that steps would typically have this height.

4.2 The clean surfaces

LEED patterns of both surface terminations are shown in Fig. 5, and match the previously published results [21–23]. When annealing the (1×1) surface in UHV while doing LEED, the (2×1) spots come in slowly without any notable changes to the (1×1) spots, indicating a reconstruction process with only few nucleation events compared to the speed of domain growth, as previously reported by Henderson [23, 24].

For the (1×1) termination, one would expect a glide plane along the $[12\bar{1}]$ directions in a bulk terminated model. When measuring LEED, this should result in every other diffraction spot missing along the main axis in that direction at all electron beam energies. In experiments, these spots are observed missing at most, but weakly visible at some energies. This indicated either that the glide plane symmetry is not fully realized, or that the angle of incidence of the electron beam is not quite perpendicular. In either case, the same spots are observed to be missing or only weakly present in the (2×1) surface LEED patterns. It is therefore reasonable to assume that the reconstructed surface will also possess a glide plane symmetry along the $[12\bar{1}]$ direction.

STM images of the clean (1×1) surface in positive and negative bias are shown in Fig. 6. In both images, bright zig-zag rows in the $[12\bar{1}]$ direction are clearly resolved. The measured unit cell has the expected size of $5.0 \times 5.4 \text{ \AA}$, with two nooks in each unit cell, which assumedly correspond to one surface atom each. At least some of the defects are probably caused by water, which is always present in the residual gas and dissociates readily on the surface, as will be discussed in chapters 4.3 and 4.4.

The defects in the STM images can be used to superimpose their features and evaluate their position in respect to each other. The defects that are positioned on the bright lines in Fig. 6 (a) are found to be between the line in Fig. 6 (b), and vice versa, suggesting that whatever

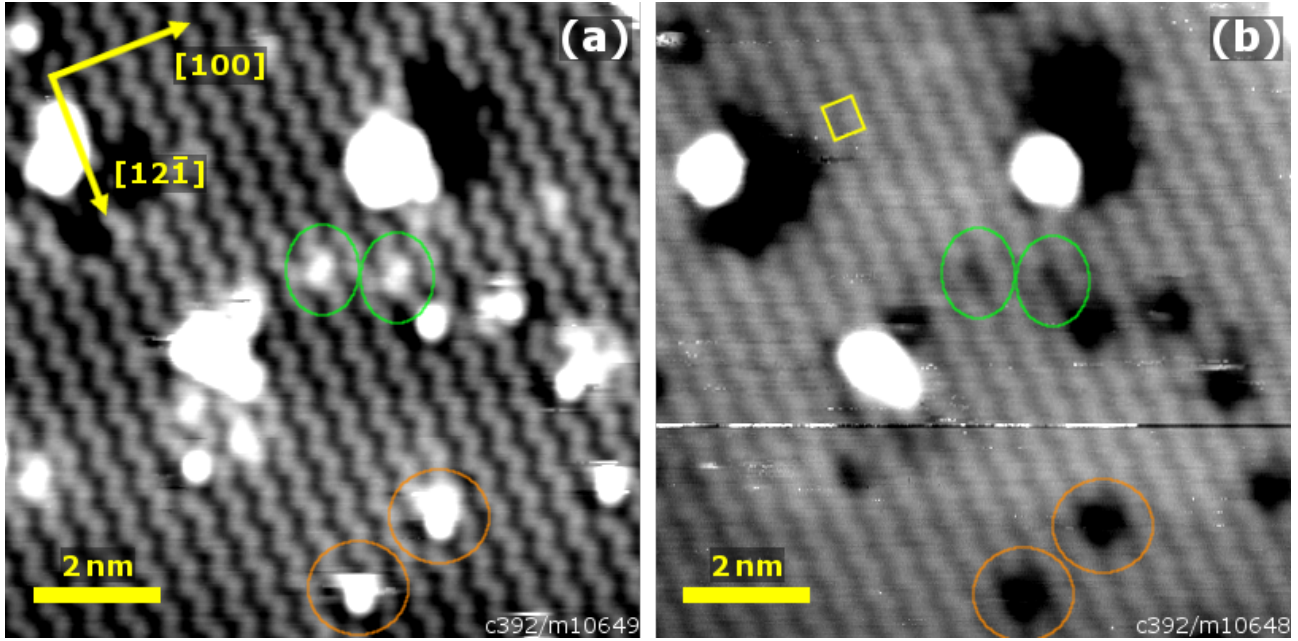


Figure 6: $10 \times 10 \text{ nm}^2$ STM images of the (1×1) $\alpha\text{-Fe}_2\text{O}_3(012)$ surface. (a) filled states image, $U = -3 \text{ V}$, $I = 0.1 \text{ nA}$. (b) empty states image, $U = +3 \text{ V}$, $I = 0.1 \text{ nA}$. The defects marked in green are located on the bright zig-zag lines in (a) but between the lines in (b), while the defects marked in orange are located between the lines in (a) but on the lines in (b), indicating that different species are imaged depending on bias.

species is imaged as bright in positive bias is dark in negative bias. Since both iron and oxygen are arranged in zig-zag rows in the bulk-terminated model, it is reasonable to assume that one image shows the oxygen anions and the other image shows the iron cations.

Filled and empty states STM images of the clean (2×1) surface are shown in Figs. 7 and 8. The images shown in Fig. 7 are on a larger scale and show paired rows of features in the $[12\bar{1}]$ direction, with a phase shift of every other row and a more pronounced gap between each pair, which causes the (2×1) periodicity. The unit cell is twice as wide as on the (1×1) surface, which is the expected result. Again, using a defect species that is clearly recognizable and localized in both images, the positions of the main features can be compared. Since the defects marked in green in Fig. 7 are each on one pair of rows in both the filled and the empty states image, it seems like the features can be attributed to the same atomic species in either case. The more common, highly mobile defect species, imaged as dark lines in the filled states image and as bright spots in the empty states image, is probably dissociated water, as will be shown in chapter 4.3.

Fig. 8 shows higher resolution images of the (2×1) surface. The $c(2 \times 1)$ structure of the round features composing the paired rows is much more clearly resolved in the filled states image, but is also recognizable for the empty states. The number and overall arrangement of the features is the same in both images, which further strengthens the argument that they represent the same species. Again, the mobile defect species imaged as dark in negative bias and as bright in positive bias is probably dissociated water.

It is worth noting that the pairing of the rows is much less pronounced in Fig. 8 than in Fig. 7, and it is generally true that how clearly the darker gaps can be seen depends strongly on bias and tip termination. While it might seem at first glance as if the gaps represent a larger distance in the $[100]$ direction between the neighbouring rows, images like the one shown in

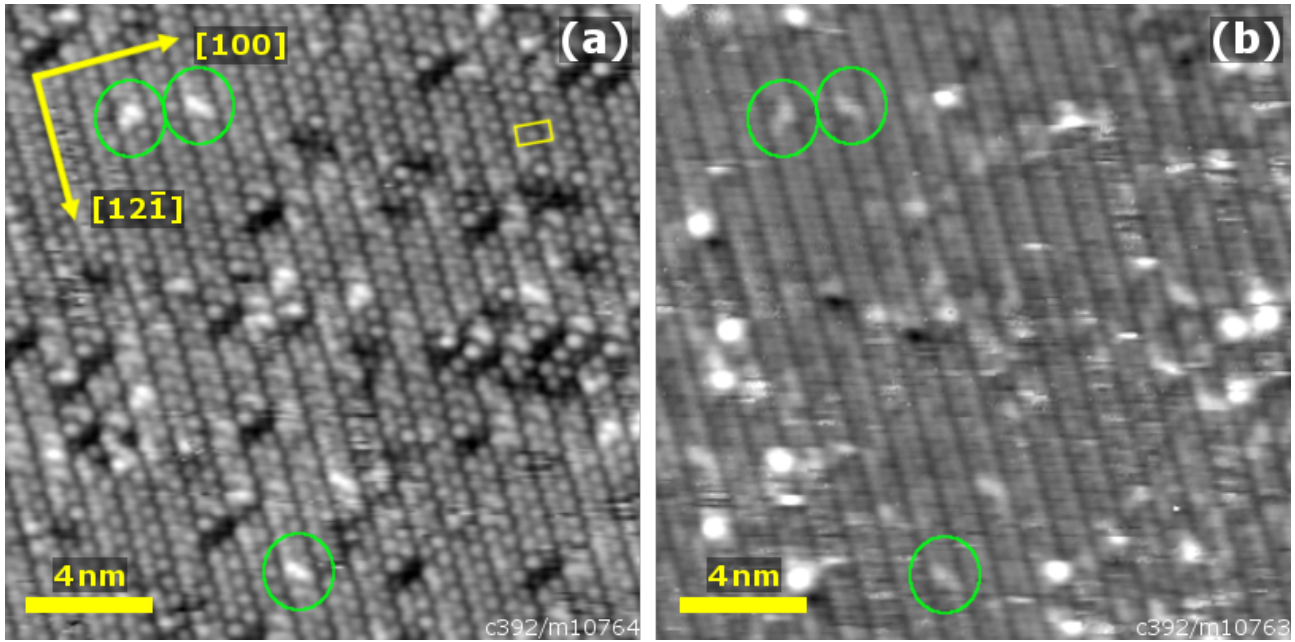


Figure 7: $20 \times 20 \text{ nm}^2$ STM images of the (2×1) surface of $\alpha\text{-Fe}_2\text{O}_3(012)$. (a) filled states image, $U = -2.5\text{V}$, $I = 0.1\text{nA}$. (b) empty states image, $U = +2.5\text{V}$, $I = 0.1\text{nA}$. The defects, marked in green, indicate that the same species is imaged in both filled and empty states, forming a roughly $c(2 \times 1)$ pattern of paired lines with a more pronounced gap between the pairs.

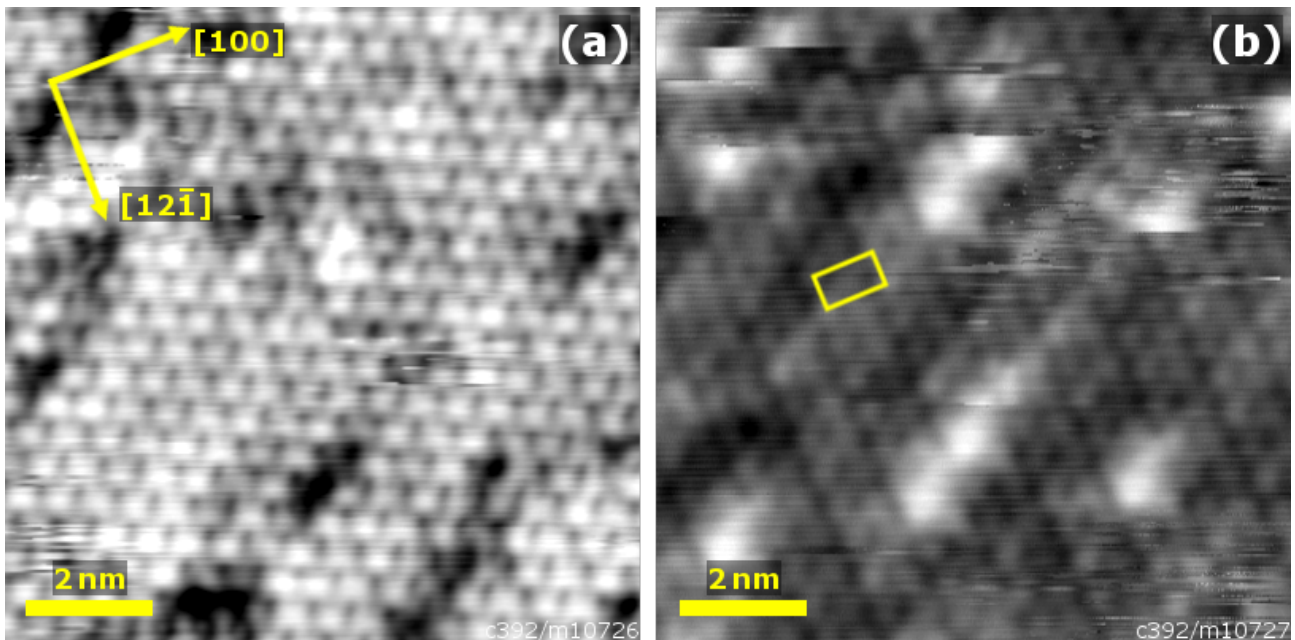


Figure 8: $10 \times 10 \text{ nm}^2$ STM images of the (2×1) $\alpha\text{-Fe}_2\text{O}_3(012)$ surface. (a) filled states image, $U = -1 \text{ V}$, $I = 0.1 \text{ nA}$. (b) empty states image, $U = +2 \text{ V}$, $I = 0.1 \text{ nA}$. Round features are arranged in a roughly $c(2 \times 1)$ pattern, with the same number and overall arrangement of features in both images.

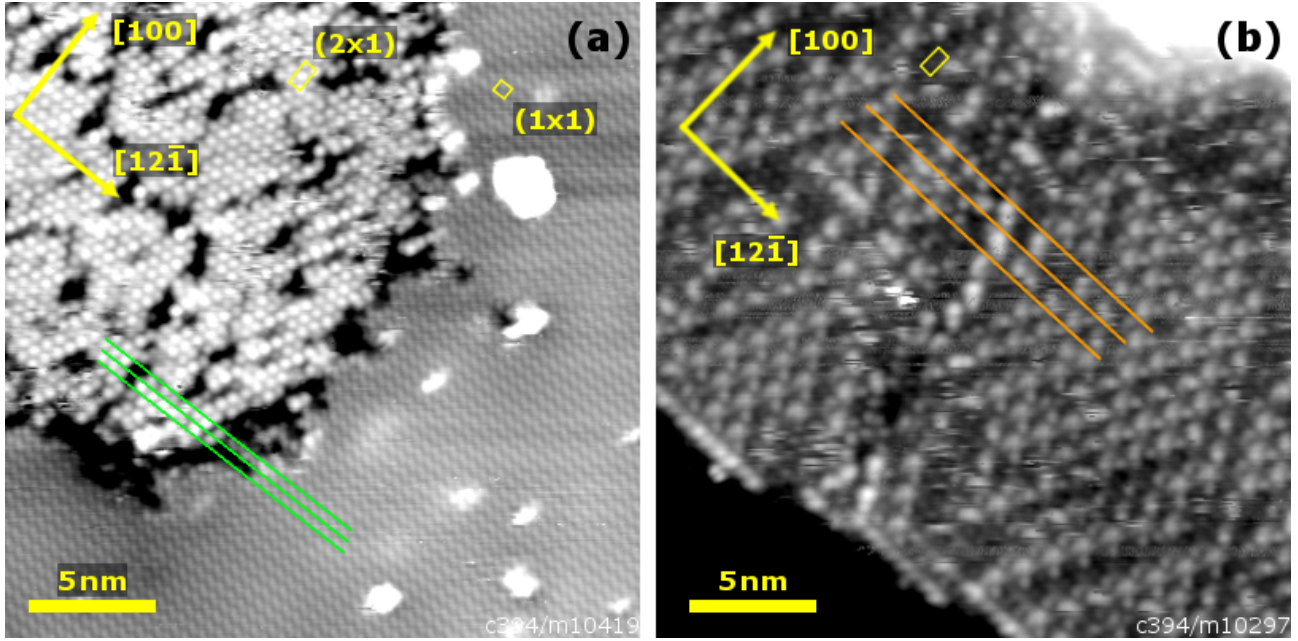


Figure 9: (a) $25 \times 25 \text{ nm}^2$ STM image (filled states, $U = -2 \text{ V}$, $I = 0.1 \text{ nA}$) of a phase boundary between the (1×1) and the (2×1) surface termination. Each zig-zag row on the (1×1) surface is continued by a row of round features on the (2×1) surface, as indicated by the green lines. (b) $25 \times 25 \text{ nm}^2$ STM image (empty states, $U = +2 \text{ V}$, $I = 0.1 \text{ nA}$) of an interphase domain boundary on the (2×1) surface, with a superstructure of dissociated H_2O (see chapter 4.3). The rows of large adsorbates are shifted by half a unit cell in the $[100]$ direction at the phase boundary, as indicated by the orange lines.

Fig. 8 (a) might suggest that the difference in the trenches is not so much a spatial as it is an electronic effect.

A mixed surface containing both the (1×1) and the (2×1) termination can be prepared by annealing the (1×1) surface in UHV for a shorter time. An STM image of one resulting phase boundary between the (1×1) and the (2×1) termination is shown in Fig. 9 (a). Each zig-zag row imaged as bright in negative bias on the (1×1) side is found to be continued by one row of the round features on the (2×1) side, as indicated by the green lines. On the (2×1) surface, there are numerous dark features associated with adsorbed water, while the (1×1) surface is mostly clean, with some large, bright patches, assumedly also adsorbates. Slightly different heights are measured for the (2×1) and the (1×1) surface in constant current mode, but which phase appears higher depends on the bias, indicating that this is an electronic effect. Likewise, the large black trench marking the domain boundary might conceivably not be a spatial but rather an electronic feature.

An STM image of an interphase domain boundary on the (2×1) surface is shown in Fig. 9 (b). The superstructure of large adsorbates is composed of dissociated water, as will be discussed in chapter 4.3. The large features of that superstructure adsorb only in one type of the (2×1) trenches, and are shifted by half a unit cell in the $[100]$ direction at the phase boundary, as indicated by the orange lines. The underlying trench structure can also be vaguely seen, but the presence of a phase boundary can be directly construed from the arrangement of the adsorbates. It is worth noting that such interphase domain boundaries were observed only twice in the course of the measurements presented here, supporting the prediction that the growth of existing (2×1) domains happens on a small timescale compared to the emergence of new nucleation points.

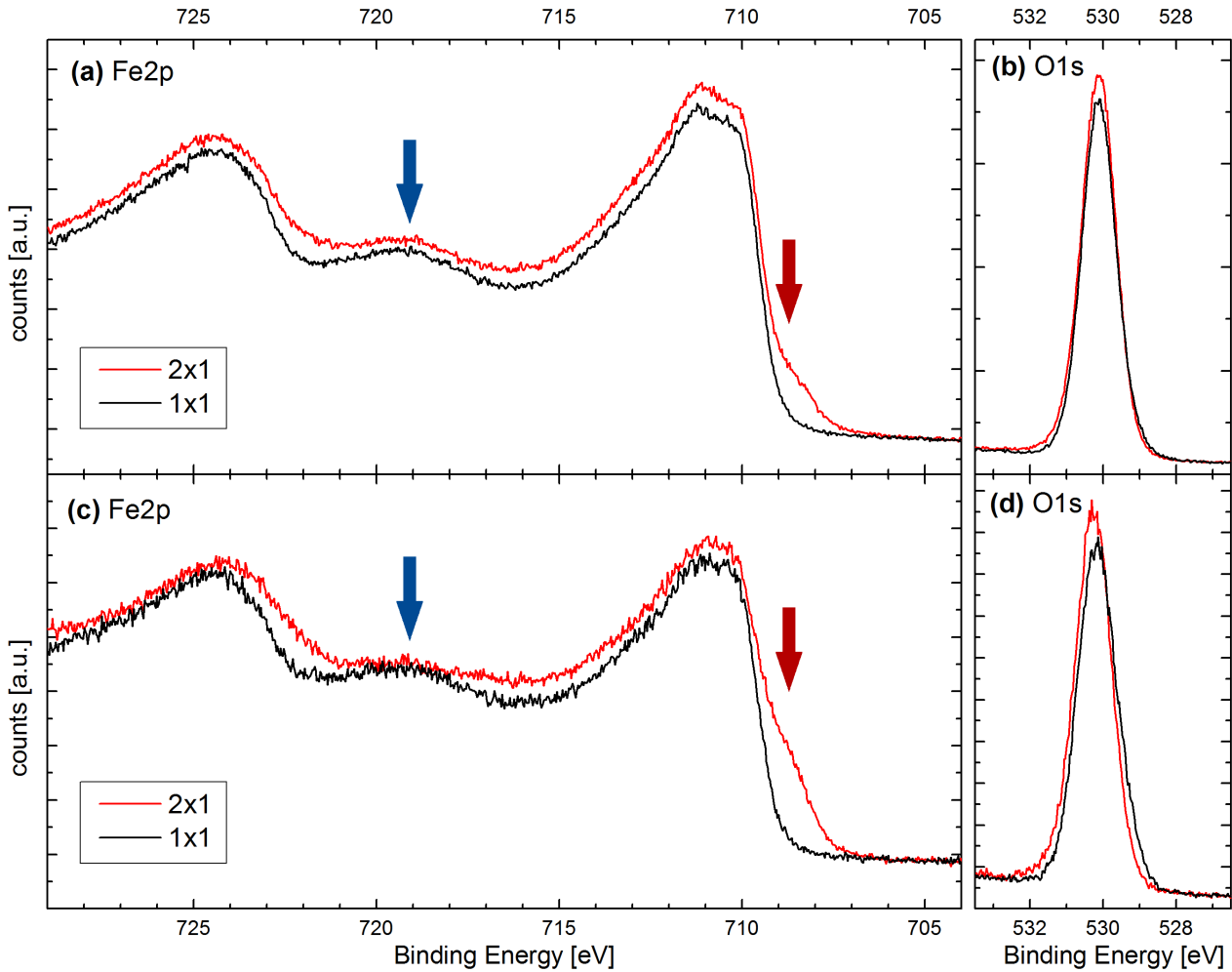


Figure 10: Normal emission (a,b) and 75° grazing emission (c,d) XPS spectra of the Fe2p (a,c) and the O1s (b,d) peaks of (1 \times 1) and (2 \times 1) terminated α -Fe₂O₃(012). The highlighted satellite peak (blue arrow) and right shoulder of the Fe2p_{3/2} peak (red arrows) indicate that Fe²⁺ cation sites are present on the (2 \times 1), but not on the (1 \times 1) surface.

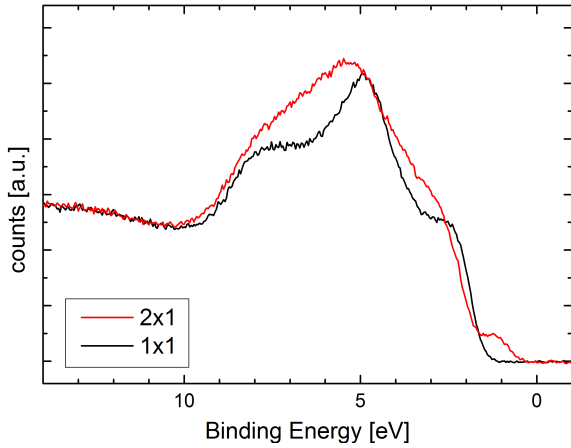


Figure 11: UPS spectrum of the valence band region using the Helium I line for the (1×1) and the (2×1) surface. The (2×1) reconstruction exhibits additional states near the Fermi level.

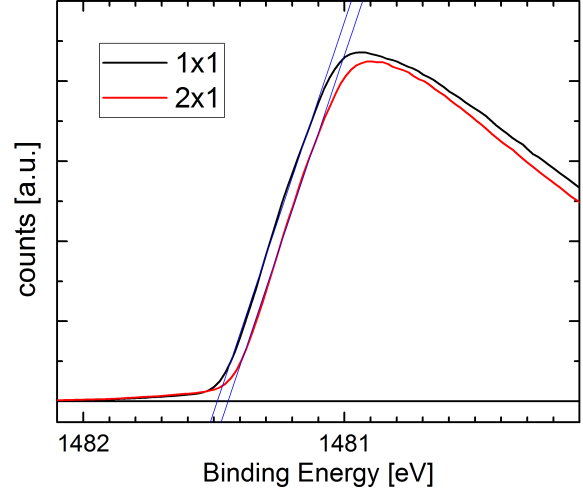


Figure 12: Low kinetic energy cutoff for the (2×1) and (1×1) surface as measured by XPS, after correcting for charging peak shift and acceleration bias.

Grazing emission XPS spectra for the O1s and the Fe2p peak are shown in Fig. 10, comparing the (1×1) and the (2×1) surface. While the O1s peaks are virtually identical, the Fe2p spectrum for the (1×1) surface exhibits a satellite peak between the Fe2p_{1/2} and the Fe2p_{3/2} peaks, associated with Fe³⁺ cations [14, 35], which is almost non-existent for the (2×1) termination in grazing emission. Meanwhile, the Fe2p_{3/2} peak has a right shoulder in the (2×1) spectrum, which is indicative of Fe²⁺ [14, 20]. While the Fe2p spectra of the (1×1) termination look the same for both normal and grazing emission, the features indicative of Fe²⁺ cations are much more pronounced in the grazing emission spectrum, indicating that these Fe²⁺ are located in the immediate surface layers.

UPS spectra of the valence band region of both the (1×1) and the (2×1) surface are shown in Fig. 11. The (2×1) surface exhibits additional states near the Fermi level and a general smearing of the distinct states of the (1×1) surface. The work function was measured both by UPS and by XPS. The low kinetic energy cutoff in XPS, as taken with an acceleration voltage of 19.96 V, is shown in Fig. 12. However, all photoelectron spectra exhibited a different energy shift for the (1×1) and the (2×1) surfaces, probably due to differences in charging. For XPS measurements, this effect could be compensated by also measuring the position of the O1s peak and shifting the entire spectrum to align it with the literature value of 530.1 eV binding energy [20]. This yields a work function of 5.2(6) eV for the (1×1) surface and 5.3(0) eV for the (2×1) surface. The work function was also measured with UPS, which yielded a work function difference of ≈ 0.1 eV, but in the absence of peaks with known binding energy, there is no way to correct for charging shift, so the work function measurements by XPS probably yield the more reliable results.

Atomic force microscopy (AFM) images of the clean (1×1) and (2×1) surfaces were kindly provided by Zdeněk Jakub (Institute of Applied Physics, TU Wien) and are shown in Fig. 13. The tip was prepared by scanning on a Cu sample and is presumed to be Cu-terminated. Although interpretation of the forces imaged in AFM is not straightforward, it is assumed that the bright features imaged in the insets are oxygen, while at close proximity, the tip interacts

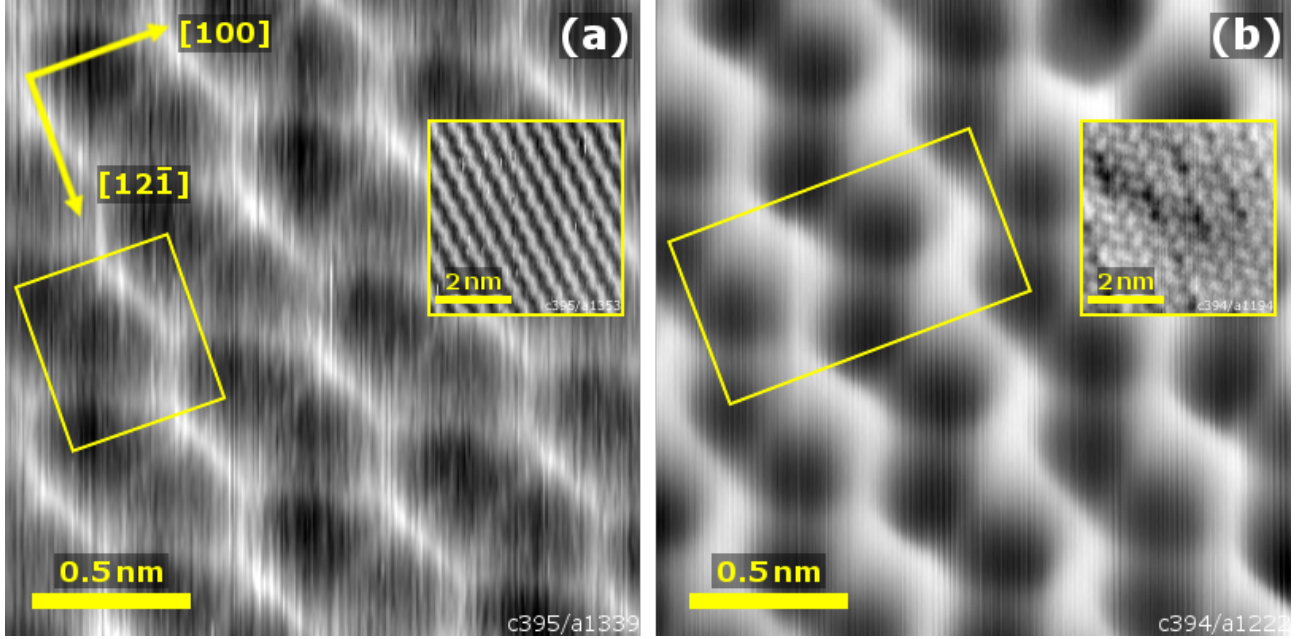


Figure 13: $2 \times 2 \text{ nm}^2$ constant height AFM images of the (1×1) (a) ($T = 78 \text{ K}$, $A = 300 \text{ pm}$) and the (2×1) (b) ($T = 5 \text{ K}$, $A = 55 \text{ pm}$) surfaces with high tip-sample proximity. The (2×1) periodicity in (b) is caused by a slight phase shift of every other row of dark features. $5 \times 5 \text{ nm}^2$ AFM images with higher tip-sample distance are shown in the insets ((a) $T = 78 \text{ K}$, $A = 300 \text{ pm}$, (b) $T = 5 \text{ K}$, $A = 500 \text{ pm}$). Images provided by Zdeněk Jakub (Institute of Applied Physics, TU Wien).

much more strongly with the Fe cations, so the dark features in the main images are attributed to iron. The remaining white features would then loosely correspond to oxygen, but due to the dominant interaction with iron, the accurate atomic position of oxygen cannot be determined from these images. It seems that the iron lattice is distorted, but basically intact on the (2×1) surface, suggesting a reconstruction based on oxygen vacancies. The distortion can be interpreted as a slight phase shift of every other iron row in the $[12\bar{1}]$ direction. The insets to Fig. 13 resemble the STM images on the clean surfaces, with continuous zig-zag lines on the (1×1) surface and separate features in a $c(2 \times 1)$ pattern on the (2×1) surface. However, the features attributed mainly to oxygen on the (2×1) surface are not round but elongated in different directions in the AFM images.

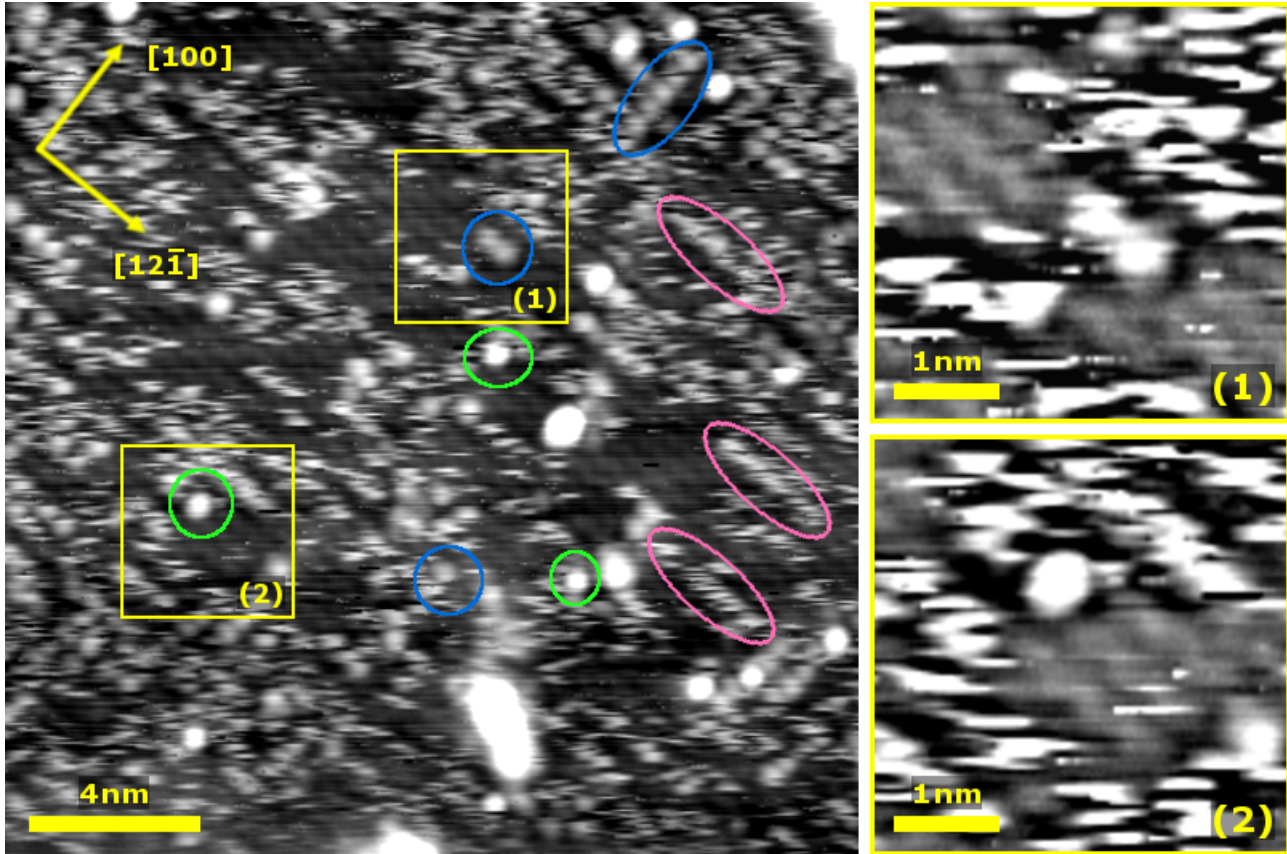


Figure 14: 20x20 nm² STM image (filled states, $U = -2.2$ V, $I = 0.04$ nA) of the α -Fe₂O₃(012) (1×1) surface after dosing 1L of water, with two areas shown enlarged with high contrast. Four species can be distinguished on top of the (1×1) zig-zag rows: A highly mobile one, marked in pink, which seems to preferentially diffuse along the $[12\bar{1}]$ direction, two stationary species with different apparent height, marked in blue and green, and finally large white features, which might be clusters of one or multiple of the other types.

4.3 Surface interaction with gaseous water

Water was dosed on the clean (1×1) and (2×1) surfaces in the RT chamber by leaking small amounts of gaseous H₂O into the vacuum. Since the sticking coefficient is unknown, the actual resulting coverage is yet to be determined. However, as will be discussed below, rapid water adsorption on the (2×1) surface was observed at room temperature even without dosing any H₂O. Since the background pressure of water was low in the chamber, the sticking coefficient must therefore be relatively high.

An STM image taken after dosing 1L of water on the clean (1×1) surface is shown in Fig. 14. Generally, scanning water on the (1×1) termination was challenging and only possible with very low tunnelling currents, which is perhaps not surprising since the desorption temperature on that surface is only slightly above room temperature, suggesting weak binding of the hydroxyls at room temperature. At first glance, Fig. 14 gives a chaotic impression due to the highly mobile adsorbates, marked in pink, which are often moved along with the STM tip. However, the zig-zag structure of the clean (1×1) surface is visible underneath, and several different types of adsorbate can be distinguished. Apart from the mobile species already mentioned, there are two types of feature which appear to be round and localized, which differ only in their apparent height. One type, highlighted here in blue, is imaged as grey and is sometimes arranged in

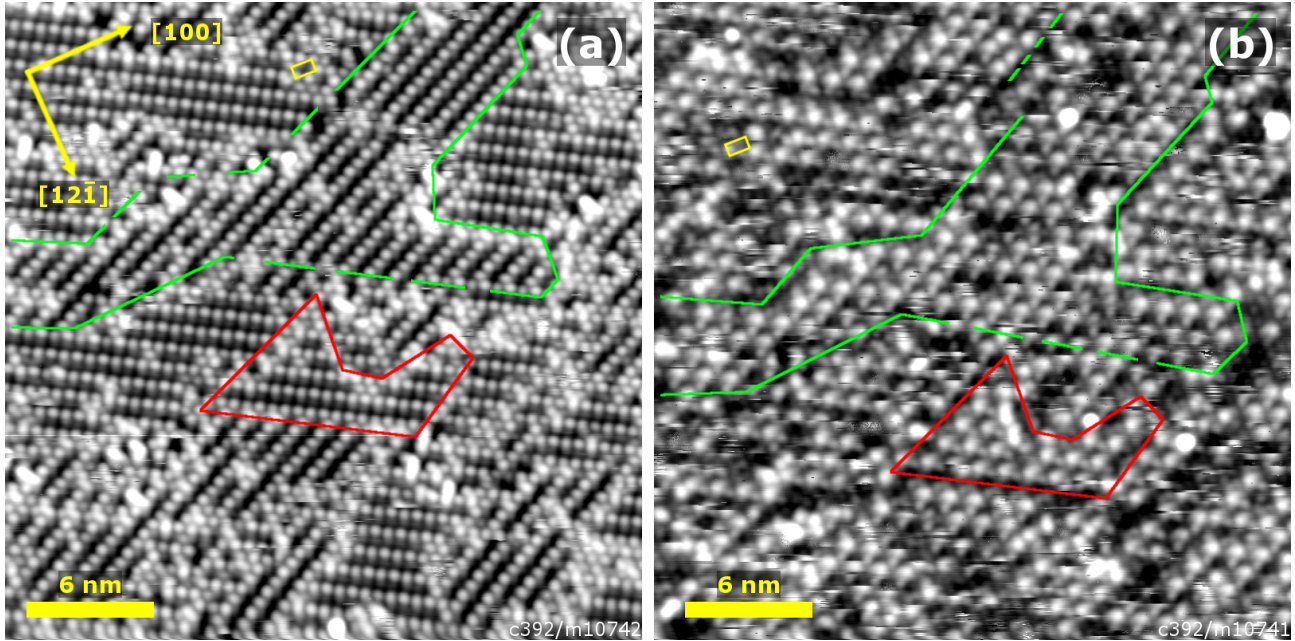


Figure 15: $30 \times 30 \text{ nm}^2$ STM images of partial water coverage on the surface of $\alpha\text{-Fe}_2\text{O}_3(012)$. (a) filled states image, $U = -2\text{V}$, $I = 0.1\text{nA}$. (b) empty states image, $U = +2\text{V}$, $I = 0.1\text{nA}$. Domains are oriented at 60° angles to the $[12\bar{1}]$ direction. The same domains are highlighted in both images, and their orientation is discernible in both positive and negative bias.

rows in the $[100]$ direction. The other type, marked in green, appears white and occurs mostly on its own. Finally, there are larger white shapes, which are often not round and might be clusters of one or multiple of the other species. As shown in the areas (1) and (2) in Fig. 14, both localized round defect species appear to be situated between the bright zig-zag rows of the $\text{Fe}_2\text{O}_3(1 \times 1)$ surface in the filled states image. While it is clearly difficult to judge the rest position of the mobile adsorbates marked in pink, they too appear to be located in the trenches between the bright zig-zag lines.

Water adsorbed on the clean (2×1) surface at first forms a domained superstructure of lines oriented at $\approx 60^\circ$ angles to the $[12\bar{1}]$ direction, as shown in Fig. 15. In filled states images, the adsorbate lines appear to black out features that would be visible on the clean (2×1) surface, leaving a roughly (2×1) pattern rotated by 60° . In empty states images, the adsorbates manifest as large features, each with one smaller feature next to it, with the angle between small and large feature corresponding to the domain orientation in the filled states images. The adsorbates do not occupy every (2×1) unit cell, but where they do, they appear to always be located in the same spot, with no phase shifts in the $[100]$ direction. Clearly, only one of the trench types of the (2×1) termination accommodates the adsorbates, and judging from the image shown in Fig. 15, this seems to be the less pronounced ('narrow') trenches.

For the purpose of identifying the different hydroxyl species and the way they are bound to the surface, it is educational to study a mostly clean surface with low H_2O coverage. Although water adsorption is also already visible in Figs. 7-9, one more high-resolution, large scale STM image of a low coverage of water on the (2×1) surface is shown in Fig. 16. In the main image, the (2×1) pattern of the clean surface and the blacked-out lines are clearly visible, but the different trenches are not discernible. A subsequent image taken with the same scanning parameters after a change in tip termination is shown in the inset, where the paired lines are

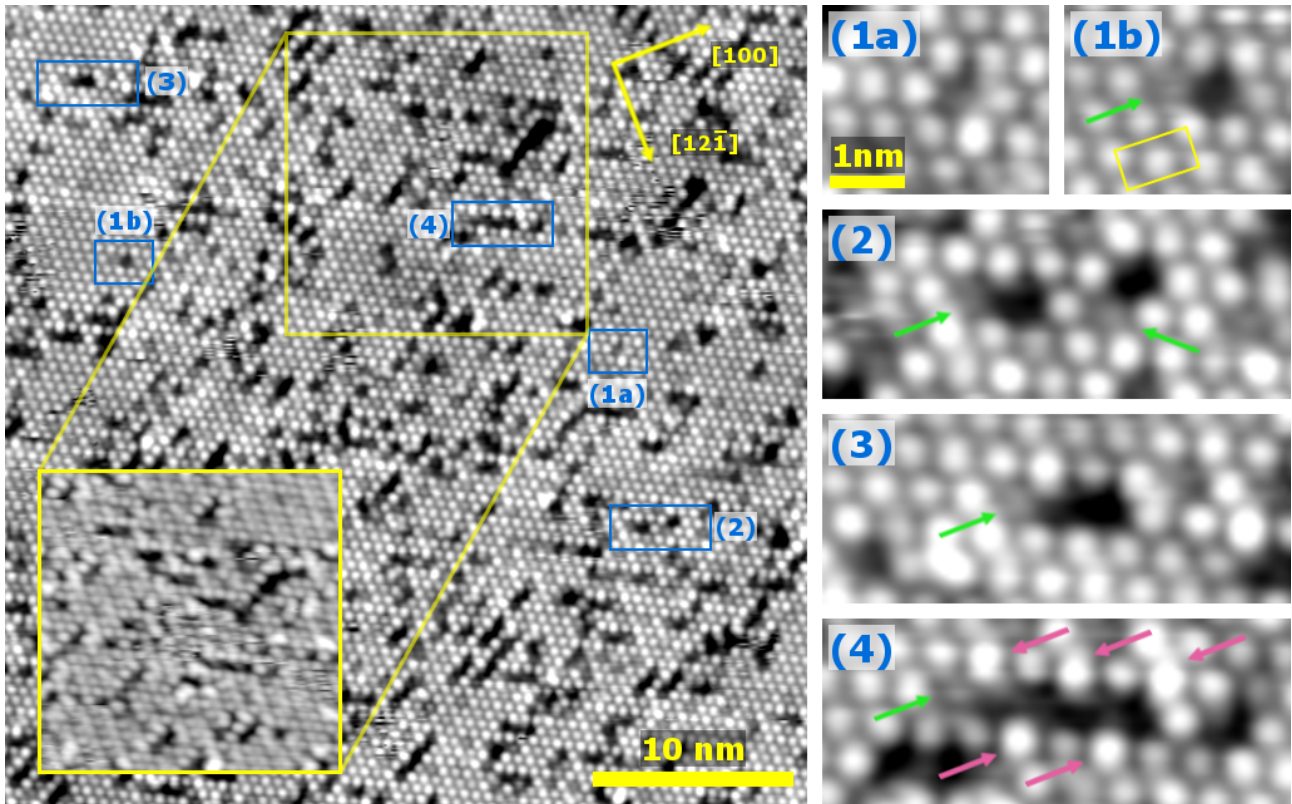


Figure 16: $40 \times 40 \text{ nm}^2$ STM images of the clean (2×1) surface with beginnings of the domained surface due to partial water coverage (filled states, $U = -2\text{V}$, $I = 0.1\text{nA}$). A subsequent image of the same area, taken with the same scanning parameters but with a differently terminated tip, in which an additional white adsorbate species is observed and the different trenches are discernible, is shown in the inset. Selected areas are shown enlarged on the right-hand side. The blacked-out lines are usually terminated by a grey feature on at least one side, as indicated by the green arrows, and sometimes weak grey features are seen along the lines. Once longer domain lines are formed, an ordered array of brighter features is often observed along the remaining bright lines, as indicated by the pink arrows in (4).

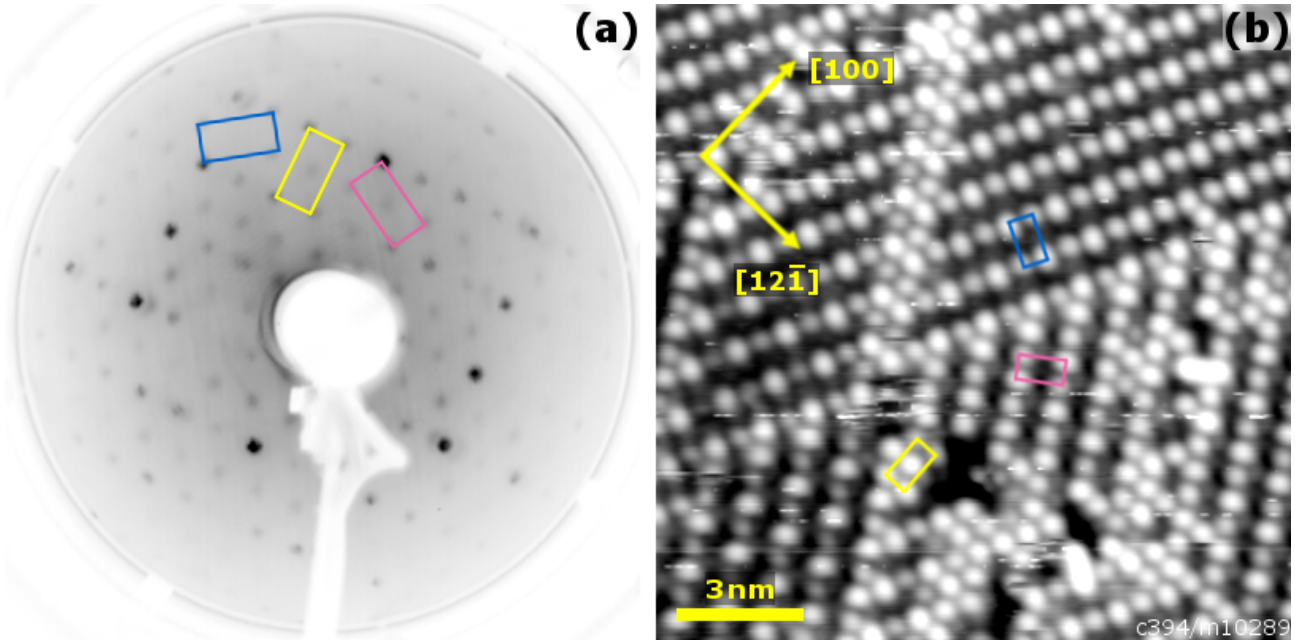


Figure 17: (a) LEED pattern of the domained H_2O superstructure on the clean (2×1) surface (electron beam energy = 150eV). (b) corresponding $15\times 15 \text{ nm}^2$ STM image (filled states, $U = -2\text{V}$, $I = 0.1\text{nA}$). The unit cell of the clean (2×1) surface is marked in yellow, while the rotated unit cells of the domained superstructure are drawn in blue and pink on both images.

clearly visible, as well as a white adsorbate species that is hidden in the main image. Concerning the dark lines, it appears that one feature of the (2×1) structure can either be completely blacked out or only greyed out by the adsorbates. Where multiple dark features occur next to each other, a black line is created, which is usually terminated by a grey feature on at least one side, as indicated by the green arrows in Fig. 16. Once a higher concentration and ordering of adsorbates is reached, the black lines are often bordered by an ordered array of brighter white features, indicated by pink arrows in Fig. 16. This phenomenon can also be observed in Fig. 17 (b).

Corresponding to the domained superstructure created by partial water coverage of the clean (2×1) surface is a LEED pattern with an extra spot in the center of the (2×1) unit cell in reciprocal space, shown in Fig. 17. The extra spots can be understood as corresponding to the unit cells of the domained superstructure, shown in Fig. 17 (b). These rotated unit cells have a size of $(\sqrt{5} \times \sqrt{5}/2)$, with the diagonal length of $\sqrt{5}$ for an ideal (2×1) unit cell.

It should be noted that the extra LEED spots disappeared over the course of 2-5 minutes, depending on electron beam energy, during LEED measurements, indicating disordering of the H_2O superstructure by the beam.

At higher H_2O coverage, the domained superstructure is replaced first in patches, and at full coverage completely, by bright zig-zag lines in the original $[12\bar{1}]$ row direction, as shown in Fig. 18 and Fig. 19. The full-coverage zig-zag structure does not occur at any point before the surface is almost fully covered in the domained superstructure. However, when heating up to desorb parts of the water, a mixed coverage of domains, bold zig-zagging lines and entirely clean surface can be created, which is never observed when dosing water.

TPD spectra of water on the (1×1) surface are shown in Fig. 20 and qualitatively match those

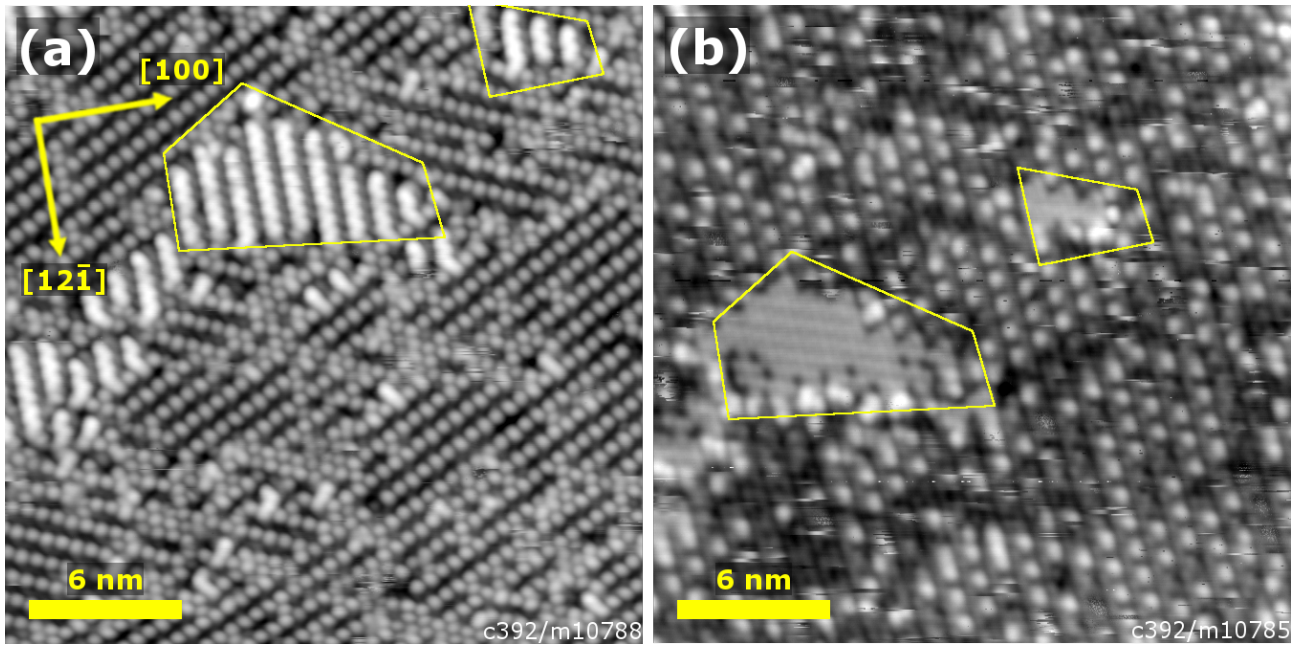


Figure 18: 25x25 nm² STM images of hydroxyls in the domained phase on the α -Fe₂O₃(012) (2×1) surface, with small patches of a new, higher-coverage phase. (a) filled states image, $U = -2.5\text{V}$, $I = 0.1\text{nA}$. (b) empty states image, $U = +2\text{V}$, $I = 0.1\text{nA}$. The same patches of the high-coverage phase are highlighted in both images.

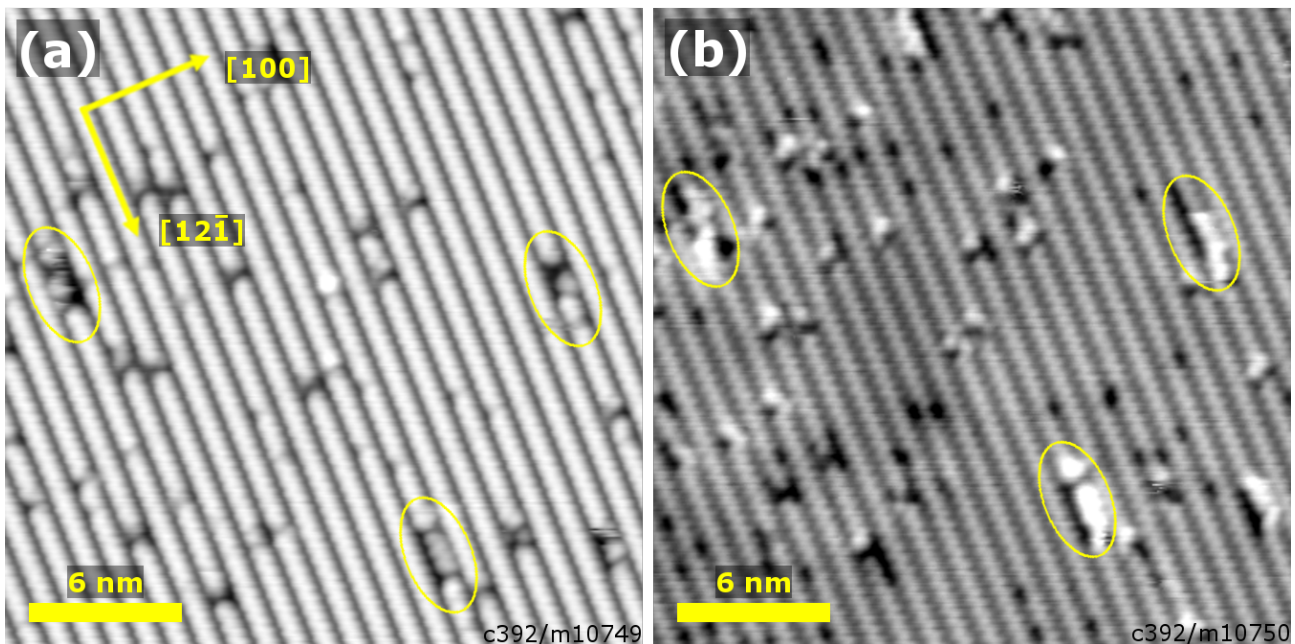


Figure 19: 25x25 nm² STM images of the α -Fe₂O₃(012) (2×1) surface with saturation water coverage at room temperature. (a) filled states image, $U = -2.5\text{V}$, $I = 0.1\text{nA}$. (b) empty states image, $U = +2.5\text{V}$, $I = 0.1\text{nA}$. The same defects are highlighted in both images.

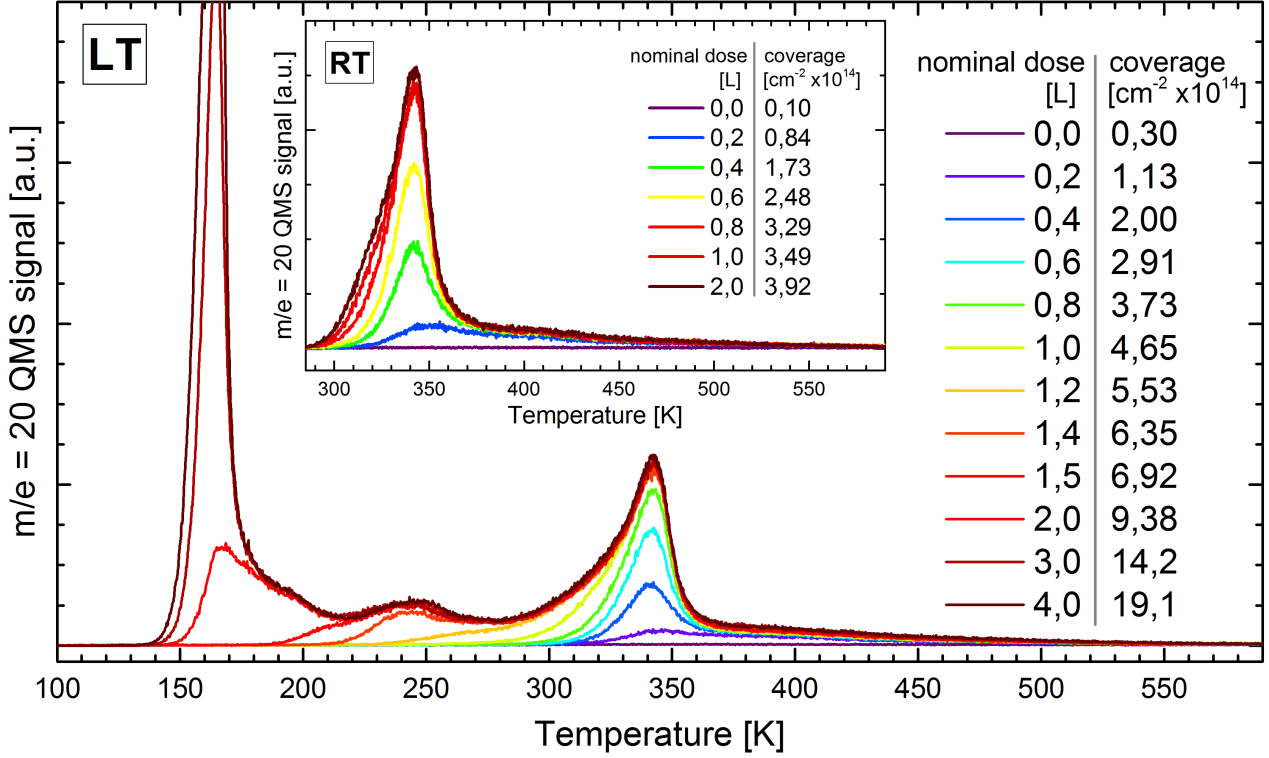


Figure 20: TPD spectra of various D₂O exposures on the α -Fe₂O₃(012) (1×1) surface, dosed at 100K (1 K/s heating rate). Inset: TPD spectra of D₂O on the same surface dosed at room temperature (1 K/s heating rate).

published by Henderson [23]. At low exposures a single peak is observed at 340 K, together with a low feature trailing to high temperatures that gets saturated almost immediately. The peak at 340 K grows with a first order behaviour, with the position of the peak maximum essentially independent from coverage and a peak asymmetry towards lower temperature. At higher coverages, a second, smaller feature grows in at 245 K, and at multilayer desorption, the multilayer peak at 165 K exhibits a right shoulder slightly below 200 K that might be another independent feature.

For better comparison to the STM experiments, TPD spectra were also taken with water dosed at 300 K, which is shown in the inset to Fig. 20. The behaviour of the feature at 340 K is essentially the same as for low temperature dosing, but the leading edge of the peak is cut off. However, no water was observed to desorb from the sample in the short timespan between dosing and starting the heating ramp.

The coverages given in Fig. 20 were calculated from the beam intensity at the sample, [36]

$$I = \frac{p_r}{k_b T} \cdot \frac{\bar{v} d_o^2}{16} \cdot \frac{1}{L^2} \cdot \gamma(\text{Kn})$$

where p_r is the pressure in the gas reservoir, \bar{v} is the average particle velocity given by the Maxwell-Boltzmann distribution, d_o is the diameter of the orifice in the gas reservoir, and L is the distance between the orifice and the exit aperture. The Knudsen number Kn is defined as $\text{Kn} = \lambda/D$, where λ is the mean free path of the particles and D is the characteristic length of a given geometry. Since the gas is not at the molecular flow limit, $\text{Kn} \gg 1$, when passing the reservoir orifice ($D = d_o$), a correction factor $\gamma(\text{Kn})$ has to be introduced [37].

A relatively uniform beam pressure at the sample and high dosing precision have previously

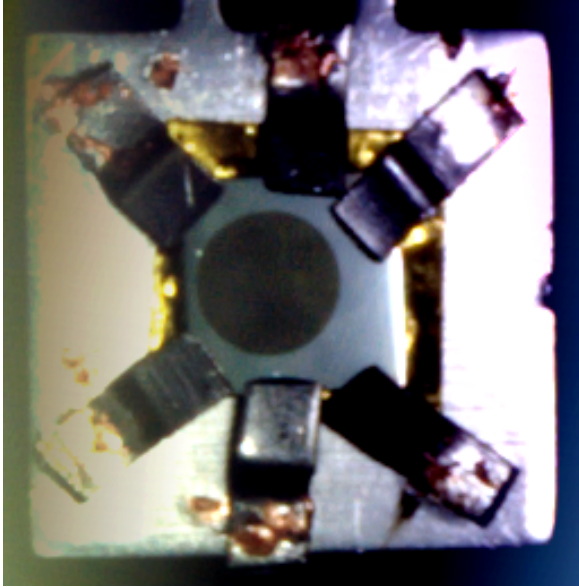


Figure 21: Contrast adjusted picture taken of the sample after dosing D_2O at 60 K for several hours. The visible layer of ice allows determination of the beam spot size.

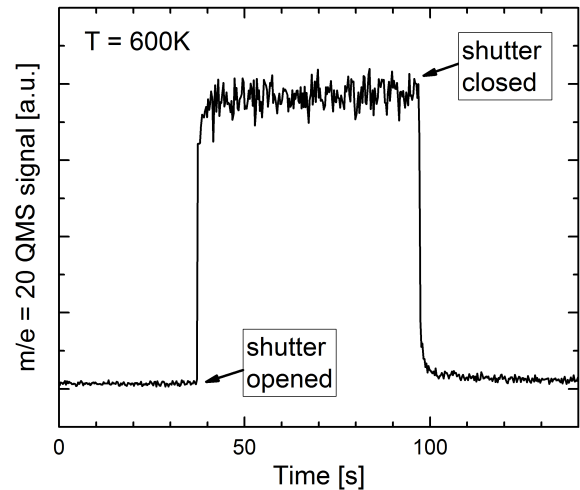


Figure 22: QMS signal while dosing D_2O on a hot sample, which should have a sticking coefficient of zero. The almost perfect hat shape confirms the high dosing precision needed to calculate the coverage after dosing.

been shown [36]. The sample position and beam geometry parameters were calibrated by dosing a thick layer of ice at low temperatures to obtain a visible beam spot, as shown in Fig. 21. The constant intensity of the beam and quick pumping of the background pressure after the beam shutter is closed can be shown by dosing on a hot sample while measuring the partial pressure with the mass spectrometer, as in Fig. 22.

From the integrated TPD area after dosing at 100 K, where the sample exhibits a sticking coefficient of ≈ 1 for D_2O , the approximate number of water molecules per unit cell can be calculated. For the TPD spectra shown in Fig. 20, this yields ≈ 1.52 molecules per (1×1) unit cell for the saturated peak at 340 K when dosing at low temperatures, and ≈ 1.90 molecules per (1×1) unit cell ($6.92 \cdot 10^{14} \text{ cm}^{-2}$) before the multilayer peak starts growing. However, when dosing at room temperature, the peak shown in the inset to Fig. 20 saturates at ≈ 1.07 molecules per unit cell, far below the capacity of even the highest temperature peak.

Calculated coverage as a function of nominal dose is shown in Fig. 23 for both the (1×1) and the (2×1) surface. The sticking coefficient is extremely high even for room temperature dosing on both surfaces at low coverages. On the (1×1) surface, sticking stays high until almost at saturation coverage, while for the (2×1) surface, sticking levels off quickly and becomes small for higher coverages.

XPS spectra of the O1s region after different amounts of D_2O have been dosed on the (1×1) surface are shown in Fig. 24. Clear peaks from both molecular and dissociated water grow in parallel starting from even the lowest coverages when dosing and measuring at low temperature. After dosing at room temperature or after dosing at low temperature and then heating to room temperature, both dissociated and molecular water remain. However, heating through the 340 K TPD peak to 375 K yields what appears to be only dissociated water on the otherwise clean surface, which corresponds to the long high temperature tail of the TPD curves.

TPD spectra of D_2O dosed at 100 K on the (2×1) surface are shown in Fig. 25. Again, they match qualitatively to the data published by Henderson [23], but exhibit a much more

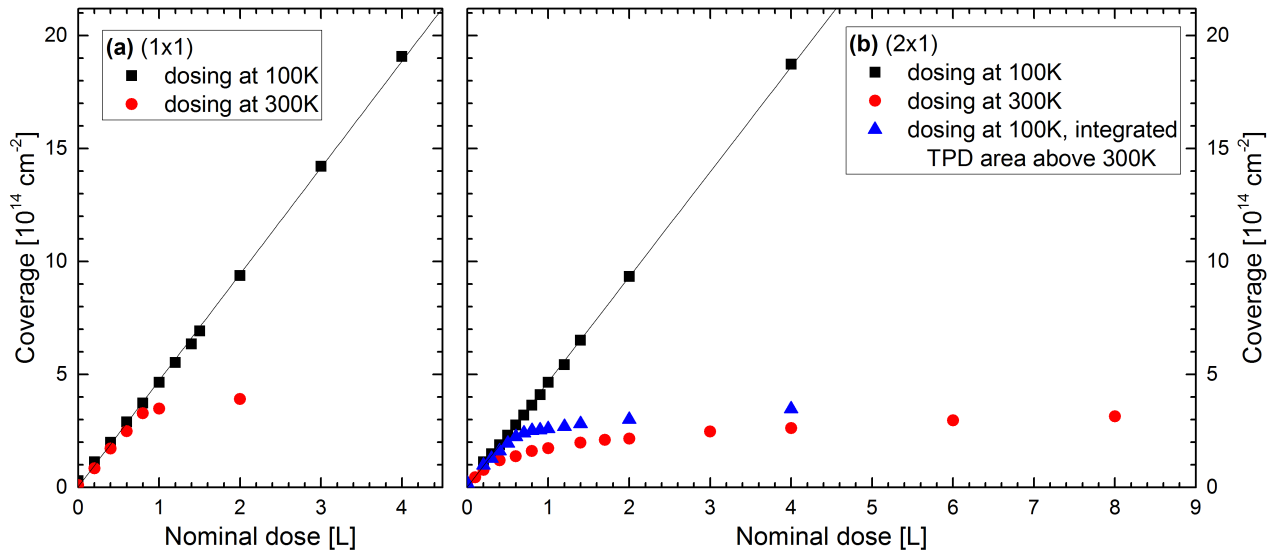


Figure 23: Coverage as a function of nominal dose for the (1 \times 1) and the (2 \times 1) surface. In (b), coverage calculated from the integrated TPD area above room temperature (300-590K) is also shown for low temperature dosing.

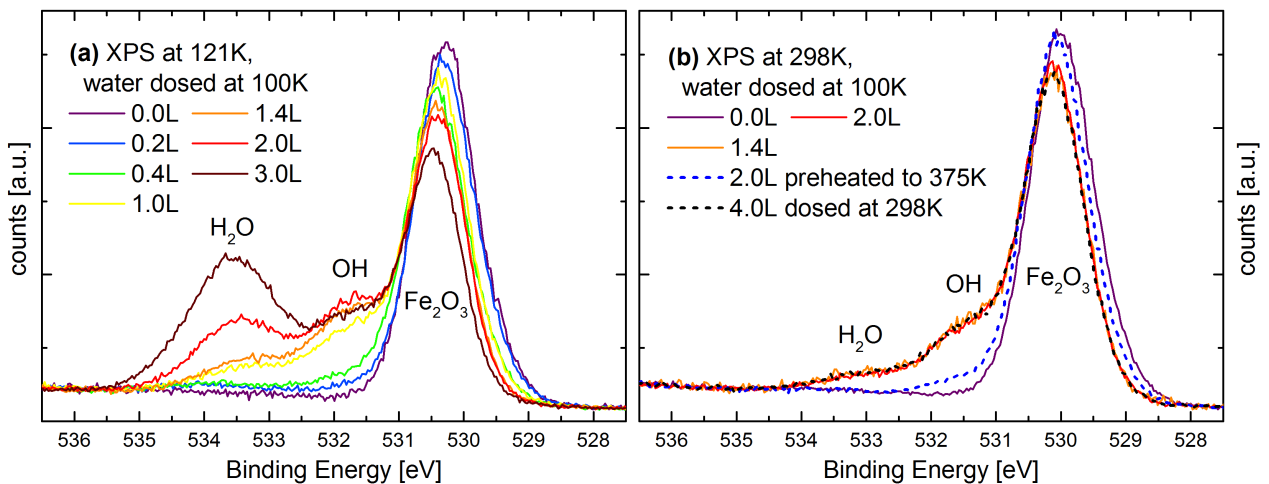


Figure 24: 75° grazing emission XPS spectra of the O1s region with different amounts of D $_2$ O dosed on the α -Fe $_2$ O $_3$ (012) (1 \times 1) surface at 100 K. (a) XPS taken at 121 K, (b) XPS taken after sample has been heated to room temperature.

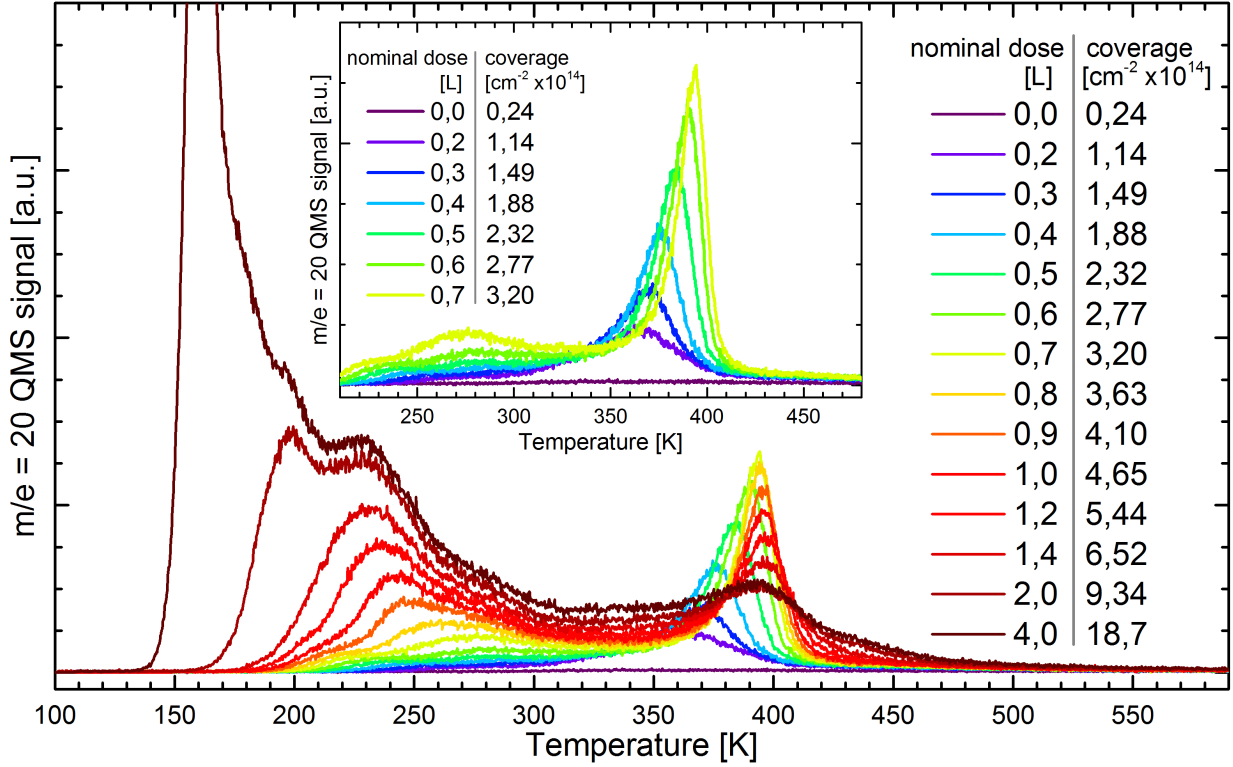


Figure 25: TPD spectra of various D₂O exposures on the α -Fe₂O₃(012) (2×1) surface, dosed at 100K (1 K/s heating rate). The same spectra up to the point where the maximum of the 395 K peak starts decreasing are shown again in the inset for clarity.

complicated behaviour than the TPD spectra of D₂O on the (1×1) termination. At low doses, a peak grows in at about 370 K with aligned leading edges and a maximum shifting to higher temperatures with rising coverage. This behaviour continues up to a nominal dose of 0.4 L, corresponding to ≈ 1.03 molecules per (2×1) unit cell. At higher doses, the leading edges begin shifting to higher temperatures, while the peak shape might point to zero-order desorption behaviour. The peak then reaches a maximum at a nominal dose of 0.7 L or ≈ 1.75 molecules per (2×1) unit cell, with the maximum at about 395 K, at which point a second feature starts growing in at 270 K. The next curve, with a dose of 0.8 L and ≈ 1.99 molecules per (2×1) unit cell, has the 395 K peak at roughly the same position but already slightly decreasing in height, while the low temperature feature starts shifting to lower temperatures, indicating second-order desorption. The high temperature feature subsequently keeps broadening until the low temperature peak is saturated and the multilayer peak starts growing. However, even though the maximum of the 395 K peak decreases, the total peak area above 300 K keeps increasing monotonically, as shown in Fig. 23 (b).

Since two phases were observed in STM and the unusual behaviour of the 295 K peak in TPD suggests a non-trivial interplay between those two phases during desorption, TPD spectra were also taken at different heating rates to account for possible kinetic effects. However, the heating rate does not appear to have any significant effect on TPD peak shape, as shown in Fig. 26.

To better understand how the TPD data relates to the STM images shown in Figs. 15 to 19, D₂O was also dosed at room temperature for TPD experiments. The resulting spectra are shown in Fig. 27. Again, the peak growth behaviour is unusual, with a small pre-feature growing in and saturating shortly after the main peak starts forming. The main peak then grows with

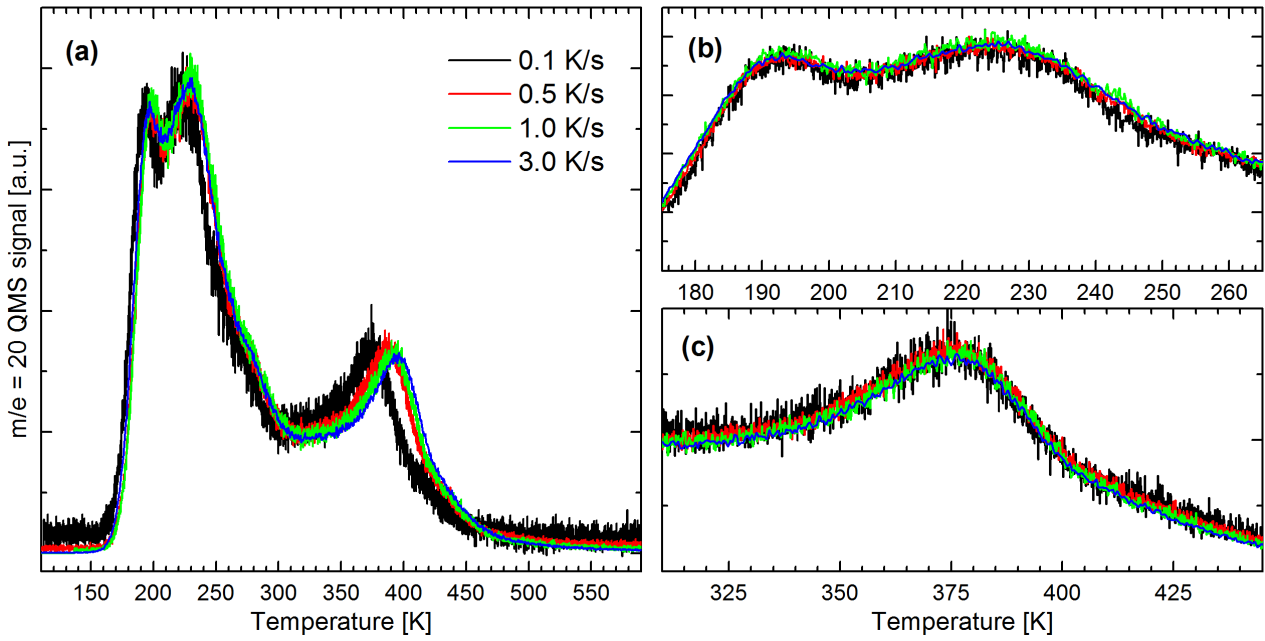


Figure 26: TPD spectra of $9.34 \cdot 10^{14} \text{ D}_2\text{O cm}^{-2}$ on the $\alpha\text{-Fe}_2\text{O}_3(012) (2 \times 1)$ surface, dosed at 100K and measured at different heating rates. (a) peak position as taken, normalized to same total peak area; low temperature features and the high temperature peak were shifted to the same maximum position for easier peak shape comparison in (b) and (c).

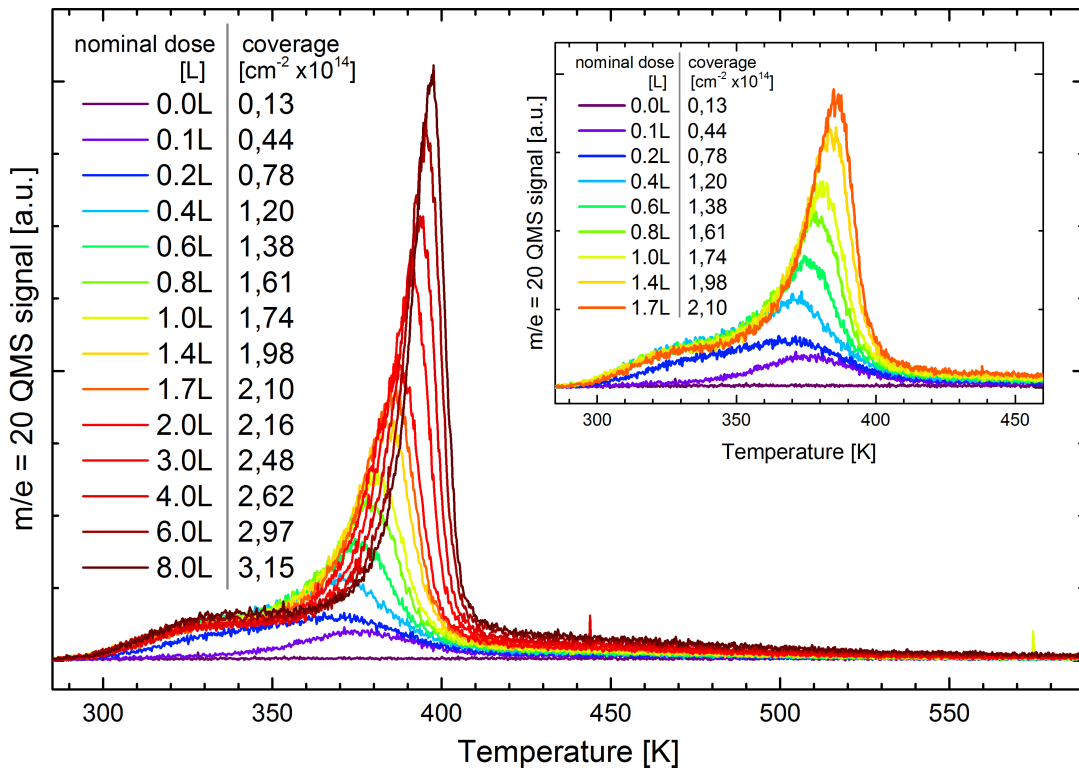


Figure 27: TPD spectra of various D_2O exposures on the $\alpha\text{-Fe}_2\text{O}_3(012) (2 \times 1)$ surface, dosed at 300K (1 K/s heating rate). The same spectra up to the point where the leading edges start shifting to higher temperatures are shown again in the inset for clarity.

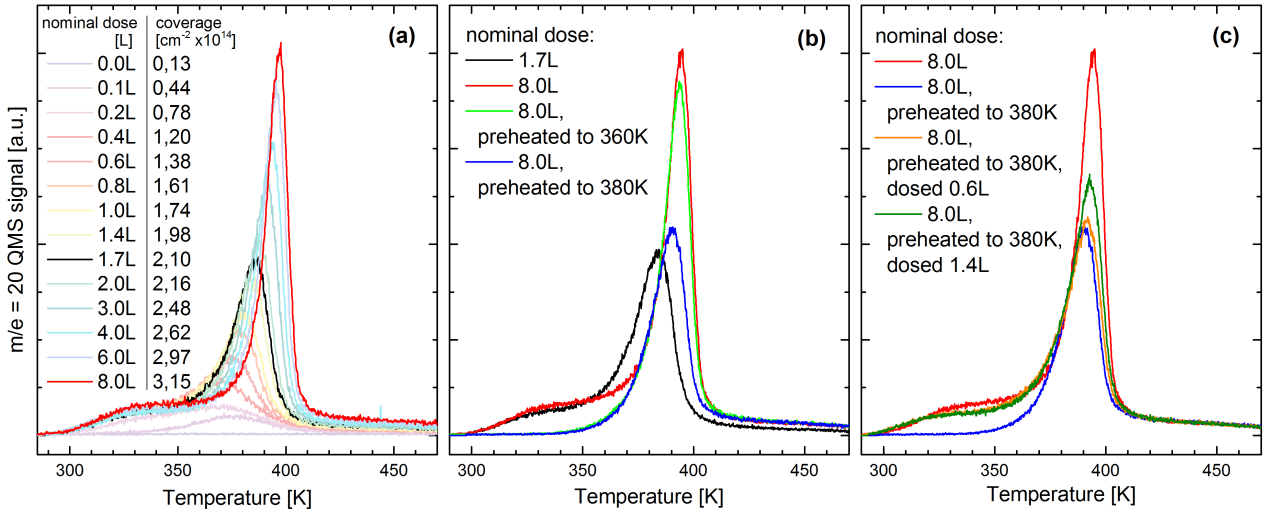


Figure 28: (a) TPD spectra of D_2O dosed on the (2×1) surface at 300 K as already shown in Fig. 27, with curves of what is assumed to be 'domained' and full coverage highlighted. (b) Comparison of the curves highlighted in (a) to the curves resulting from heating partly through the saturated peak, then cooling back down and starting TPD with already partially desorbed adsorbates. (c) Curves resulting from heating partly through the saturated peak as in (b), then dosing more D_2O at 300 K.

aligned leading edges up to a nominal dose of 1.4 L, which corresponds to ≈ 1.09 molecules per (2×1) unit cell. Subsequently, the leading edges start shifting to higher temperatures as they did when dosing at 100 K, until the peak saturates at a nominal dose of 8.0 L, which corresponds to ≈ 1.73 molecules per (2×1) unit cell.

Assuming that the peaks up to 1.4 L correspond to the 'domained' surface observed in STM, while the saturated peak corresponds to the saturation coverage shown in Fig. 19, an interesting question would be if one phase will transform into the other during desorption. This possibility was explored by heating partly through the saturation peak, then cooling the sample back down and measuring TPD of the resulting unknown adsorbate phase. The spectra measured in this fashion are shown in Fig. 28. Preheating to 360 K yielded a peak comparable in area to the one obtained by dosing 1.7 L, but with no pre-feature and a leading edge aligned with the full coverage peak. The full coverage phase therefore does not appear to transform back into the 'domained' phase during or after partial desorption. Preheating to 380 K almost leaves the saturated peak intact, but completely desorbs the pre-feature. Dosing more D_2O on the preheated phase tested in this way leads to a restored pre-feature, a leading edge slightly offset to lower temperatures, but also to growth of the 295K peak without shifting it to a different temperature.

XPS spectra of D_2O on the (2×1) surface both at 121 K and at 300 K are shown in Fig. 29. At low temperatures, the adsorbates form a mixed phase of both dissociated and molecular water, even at low coverages. However, unlike on the (1×1) surface, only dissociated water is left after heating the sample to room temperature. Saturation at room temperature appears to coincide with maximum height of the 395 K peak shown in Fig. 25.

A comparison of the (1×1) and the (2×1) surface with saturation coverages of D_2O at room temperature is shown in Fig. 30. The two terminations appear to have a similar capacity for dissociated water, but while the (1×1) surface also accommodates some molecular water, no molecular water peak is found on the (2×1) surface. The peak area of the D_2O peak of the

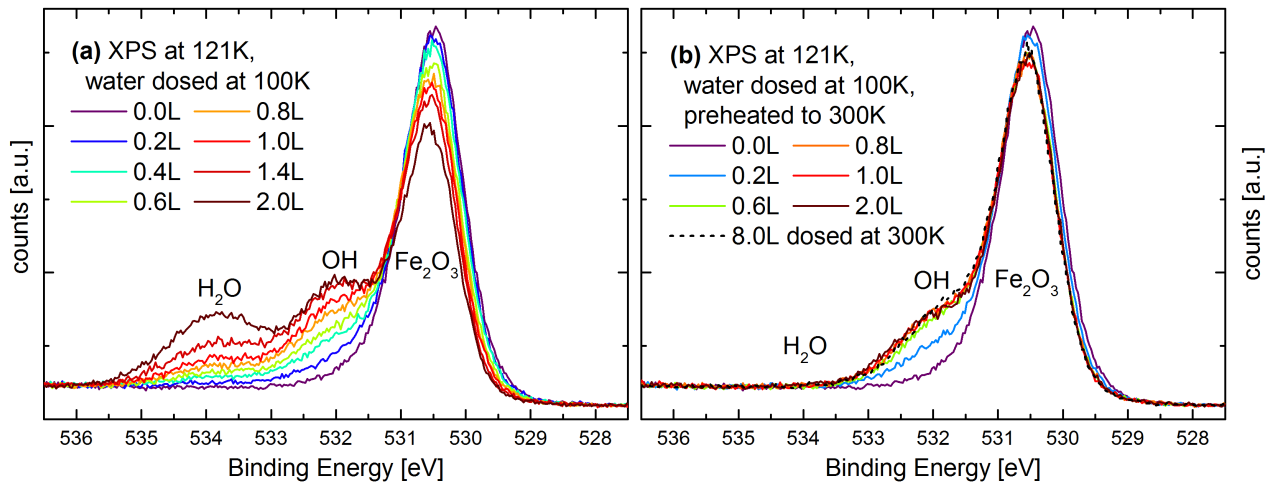


Figure 29: 75° grazing emission XPS spectra of the O1s region with different amounts of D₂O dosed on the α -Fe₂O₃(012) (2 \times 1) surface at 100 K. (a) XPS taken at 121 K, (b) XPS taken after sample had been heated to room temperature.

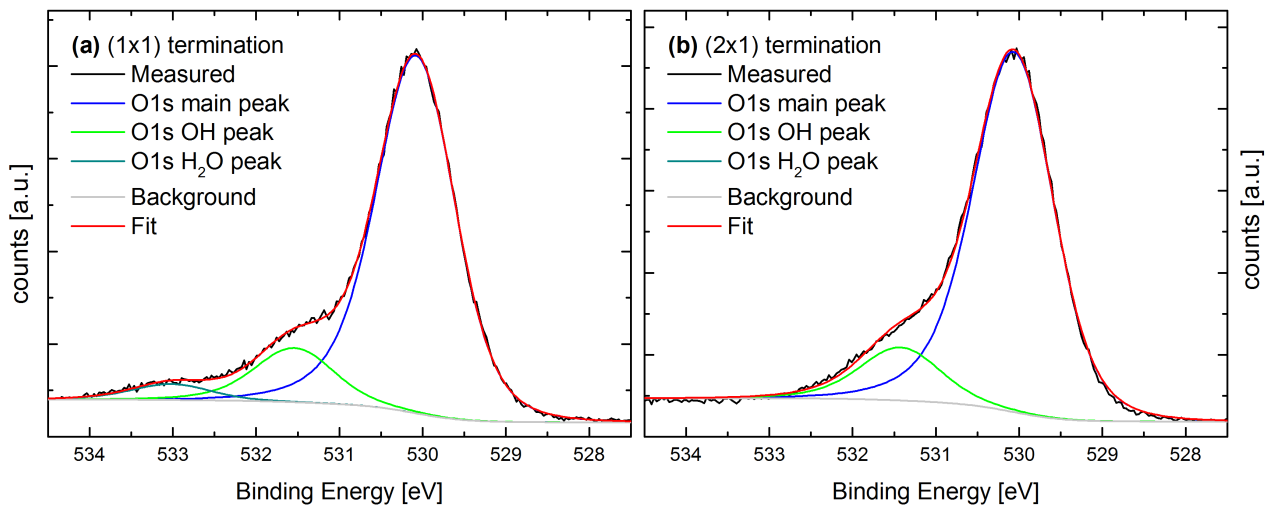


Figure 30: Fit to the 75° grazing emission XPS spectra of the O1s region with saturation D₂O coverages at room temperature for both the (1 \times 1) and the (2 \times 1) surface.

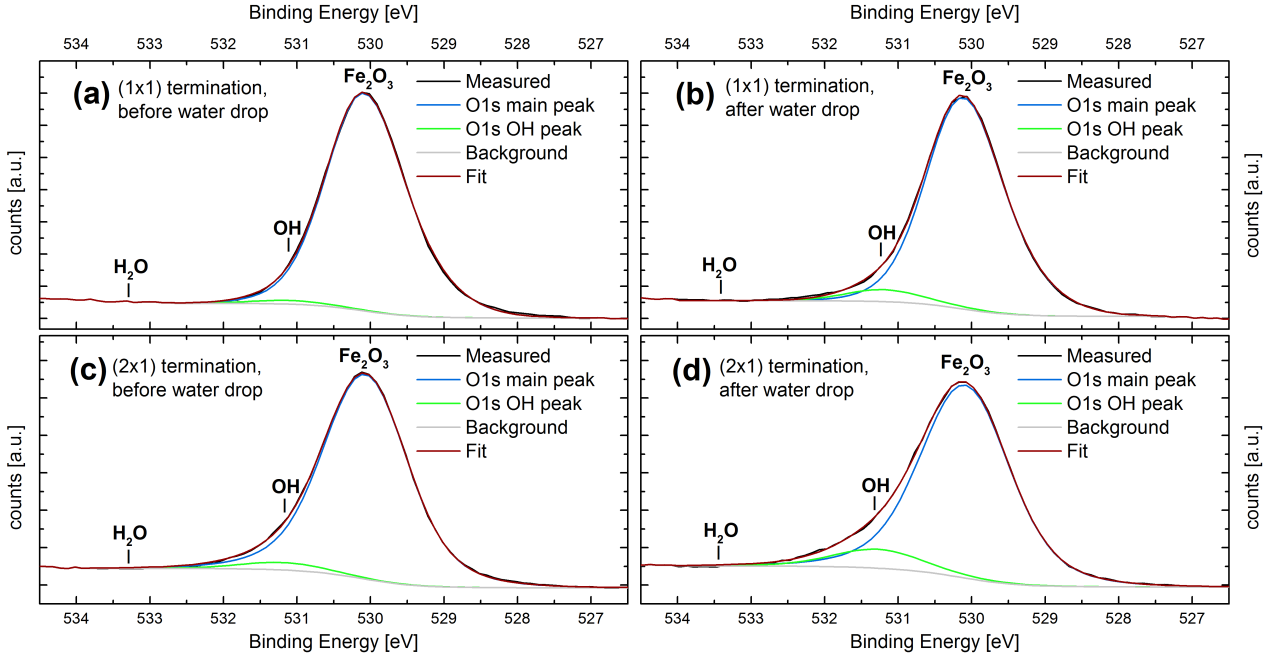


Figure 31: XPS spectra of the O1s peak on the (1×1) (a,b) and on the (2×1) (c,d) surface, freshly prepared (a,c) and after applying a drop of water (b,d). The pronounced left shoulder of the O1s main peak can be attributed to OH groups. None of the spectra exhibit a peak in the position associated with molecular water.

(1×1) surface is 29% of the OD peak area, which would mean that 37% of the adsorbed water is molecular and the remaining 63% are dissociated, since each dissociated D_2O yields twice as much XPS O1s signal as in the molecular state.

4.4 Surface interaction with liquid water

An essential step towards real application of the results presented here would be to show the agreement or disagreement of results obtained in a simplified model system, e.g. dosing water vapour in vacuum, with more realistic conditions, such as the interaction of the surface with liquid water. Water drop experiments were therefore attempted in the Omega chamber, where the loadlock containing the sample can be filled with purified argon to a pressure slightly above one atmosphere. The sample can then quickly be transferred out of the chamber, exposed to a drop of purified water, and moved back into the argon atmosphere with only seconds of contact with air. The argon, water and all other contaminants taken back into the loadlock are then pumped off as quickly as possible before the sample is transferred back into UHV. A more sophisticated setup to apply the drop without any contact to air exists, but was not used in the preliminary experiments presented here. In any case, even with the short contact to air, XPS showed only a small carbon contamination and no other contaminants on the sample after applying the water drops.

XPS spectra of the O1s region before and after applying a water drop to the (1×1) and to the (2×1) surface are shown in Fig. 31. Small dissociated water features are clearly visible after H_2O is applied, but no molecular water is observed on the (1×1) surface. However, since the OH peak is already quite small in these measurements, and the H_2O peak has been shown to have less than a third of that area, this might be due to a lack in measurement sensitivity rather than an actual difference in the adsorption behaviour. Further experiments will be required.

STM measurements of the surface after applying a water drop were also attempted, but thus far not successful.

4.5 O_2 adsorption

STM images taken on the (2×1) surface while dosing a low partial pressure of oxygen (10^{-9} – 10^{-7} mbar) into the background gas over long periods of time are shown in Fig. 32. After one hour of scanning, most of the adsorbates form patterns characteristic for dissociated water, but there are some darker areas that appear disordered in negative bias, and some bright adsorbate species not usually observed in positive bias, perhaps indicating coadsorption of water and oxygen. In Fig. 32 (e) and (f), poorly ordered adsorbates are observed next to zig-zag rows that resemble the saturated water phase shown in Fig. 19.

TPD curves for O_2 on the (1×1) surface are shown in Fig. 33. The very weak defect peak at 230 K matches data published by Henderson [31], while the much stronger low temperature features below 80 K have not been previously observed. Two small peaks saturate at one and two Langmuir nominal dose, respectively, before sharp multilayer peaks start growing.

Fig. 34 shows TPD spectra of various O_2 doses on the (2×1) termination. The curve following the initial dose has a significantly different shape than the later ones, suggesting that the surface is changed in some way. However, the signature of the later curves is different from the (1×1) spectra shown in Fig. 33, so the surface does not appear to be transformed back to the (1×1) termination. Also, this effect was not observed when dosing O_2 at 100 K, so low temperature physisorption appears to be a precondition for the process to occur. After this initial change, a weak defect feature is again observed at 210 K, in agreement with Henderson [31]. Three additional features are observed at low temperatures apart from the multilayer peak.

4.6 Effects of molecular and atomic hydrogen

Intentionally dosing molecular hydrogen had no discernible effect on either the (2×1) or the (1×1) surface. However, it must be assumed that if it is advantageous for either surface to react with molecular hydrogen, they would probably do so during preparation, since hydrogen is always present in the residual gas. Therefore, even the nominally clean surfaces might already contain some hydrogen. In any case, no change was observed when dosing additional hydrogen gas at room temperature.

A hydrogen cracker was used to dose atomic hydrogen on the surfaces. Conceptually, hydrogen gas is passed through a hot tungsten tube, and some percentage is split to $2\cdot H^0$ with the additional energy supplied in the form of heat. Neither the exact amount of atomic hydrogen that arrives at the surface is known, nor the sticking coefficient at the surface. Additionally, partial pressure measurements of H_2 gas are notoriously unreliable. Therefore, while results can be reproduced by heating the hydrogen cracker to the same temperature and dosing the same amount of H_2 gas, there is no reliable indicator of how much atomic hydrogen was actually dosed in these experiments. Interpretation of these results therefore has to refrain from any quantitative predictions.

STM images taken after dosing atomic hydrogen on a clean (2×1) $\alpha\text{-Fe}_2\text{O}_3(012)$ surface at room temperature are shown in Fig. 35. The filled states image shows dark spots, reminiscent of partial H_2O coverage, and bright spots, arranged in pairs, triplets and zig-zag lines, which resemble the superstructure observed at a full coverage of water. For interpretation, one must remember that at room temperature, rapid adsorption of water is always observed, so we cannot expect a clean surface with atomic hydrogen, but instead must anticipate a low coverage

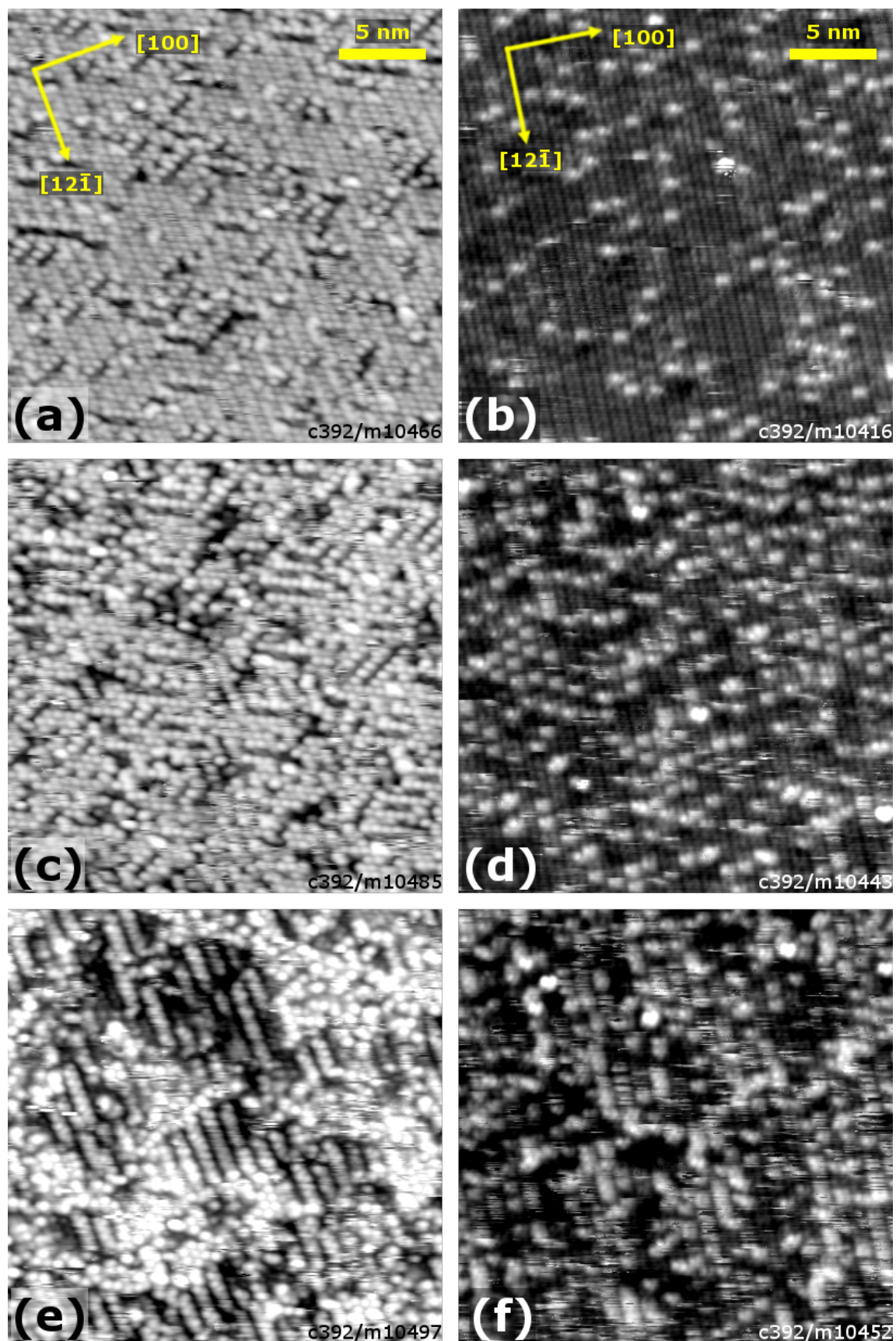


Figure 32: 25×25 nm² STM images of the (2×1) surface taken while dosing oxygen. (a,b) before dosing O₂, (c,d) after ≈ 1 hour, (e,f) after ≈ 2 hours. (a,c,e): $U = -2$ V, $I = 0.1$ nA; (b,d,f): $U = +2$ V, $I = 0.1$ nA. Scanning was done at constant bias; (a,c,e) show a different area than (b,d,f).

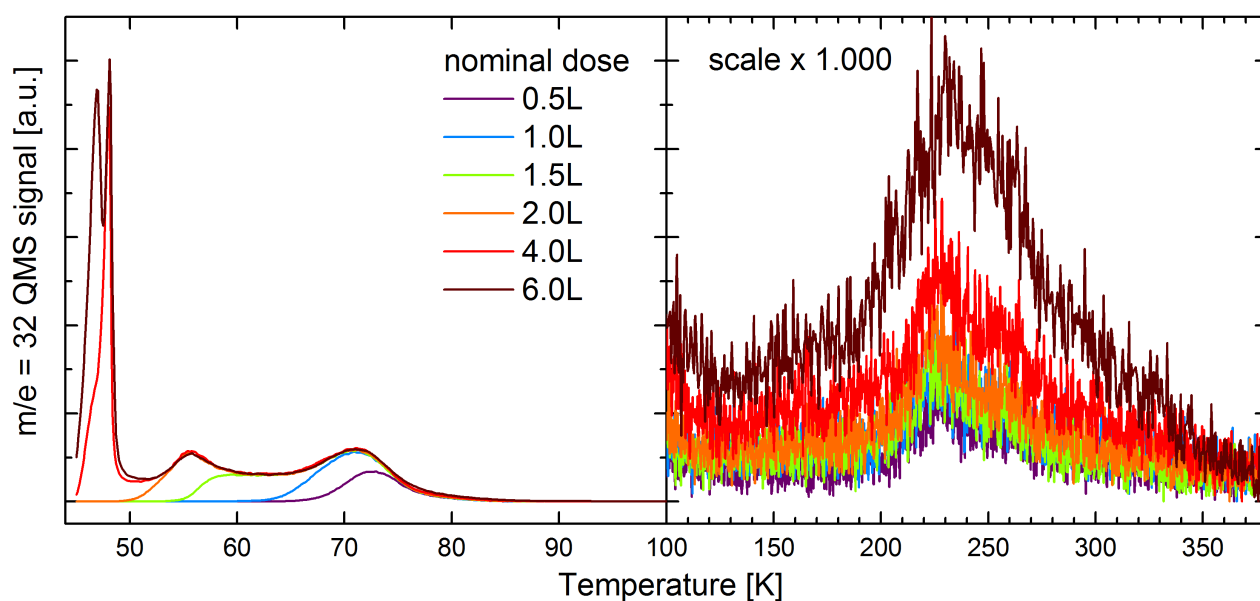


Figure 33: TPD spectra of various O_2 exposures on the $\alpha\text{-Fe}_2\text{O}_3(012)$ (1×1) surface, dosed at 43K (1 K/s heating rate). The QMS signal is shown at 1.000x the scale in the temperature range above 100 K for clarity.

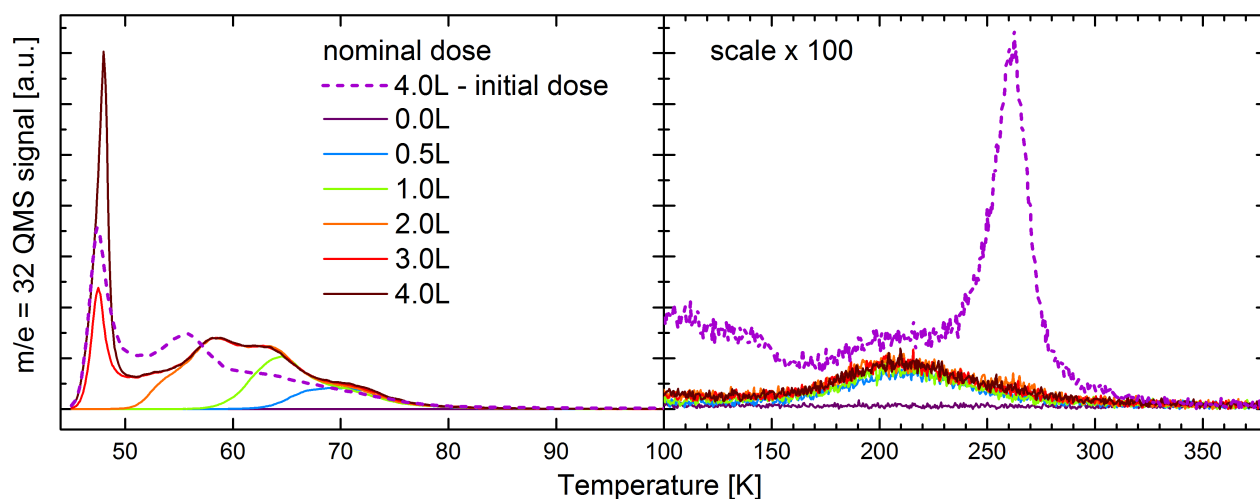


Figure 34: TPD spectra of various O_2 exposures on the $\alpha\text{-Fe}_2\text{O}_3(012)$ (2×1) surface, dosed at 43K (1 K/s heating rate). The QMS signal is shown at 100x the scale in the temperature range above 100 K for clarity.

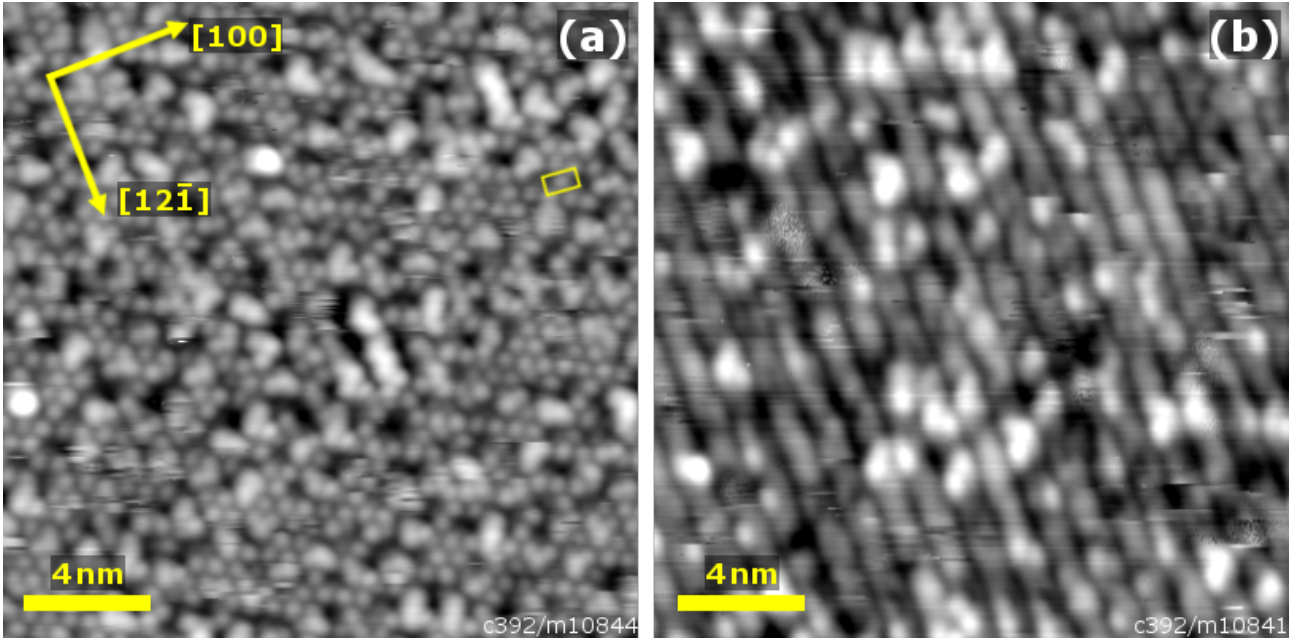


Figure 35: $20 \times 20 \text{ nm}^2$ STM images of the (2×1) $\alpha\text{-Fe}_2\text{O}_3(012)$ surface after dosing atomic hydrogen. (a) filled states image, $U = -3\text{V}$, $I = 0.1\text{nA}$. (b) empty states image, $U = +2\text{V}$, $I = 0.1\text{nA}$. Bright single spots and zig-zag lines, similar to the ones observed for full coverage of water, can be seen in both positive and negative bias. Dark spots in the filled states image resemble the beginning of a domained water overlayer, which might be due to a low coverage of coadsorbed water.

of coadsorbed water. The images should therefore be compared to measurements with some water already present, such as the one shown in Fig. 16. While dark spots and lines are always observed even with low water coverage, zig-zag lines usually do not occur before the entire surface is covered by the domained superstructure shown in Fig. 15. This effect therefore seems to be unique to the adsorption of atomic hydrogen.

Annealing the surface with adsorbed hydrogen in UHV at 150°C for five minutes yields new features in STM, shown in Fig. 36. Ordered arrays of dark spots, where on a clean (2×1) surface there would be bright round features, are found in the filled states image, and can be recognized in the empty states image as well. Some of these features are arranged in lines at angles that previously did not stand out, differing from the usual $[12\bar{1}]$ row direction and the $\approx 60^\circ$ angles of the low coverage H_2O overlayer.

4.7 Ti adatoms

Titanium was deposited via an evaporator calibrated with a quartz microbalance. One monolayer was defined as one Ti atom per (1×1) unit cell. Fig. 37 (a-c) show STM images of Ti on the clean (2×1) surface immediately after depositing, after annealing to 150°C and after annealing to 200°C . Directly after deposition, the adatoms appear to arrange in the centre of the 'narrow' trenches, in most cases with a spacing of at least one unit cell in the $[12\bar{1}]$ direction between them. After annealing to 150°C , some small clusters form, and the (2×1) surface appears disordered in some places. Finally, after annealing to 200°C , we observe both one-dimensional chains in the $[12\bar{1}]$ direction and islands growing on the surface. The step height of the islands appears to be the same as the step height of bulk hematite, and their surface structure appears to match the (2×1) termination in Fig. 37 (d), where one ML of Ti

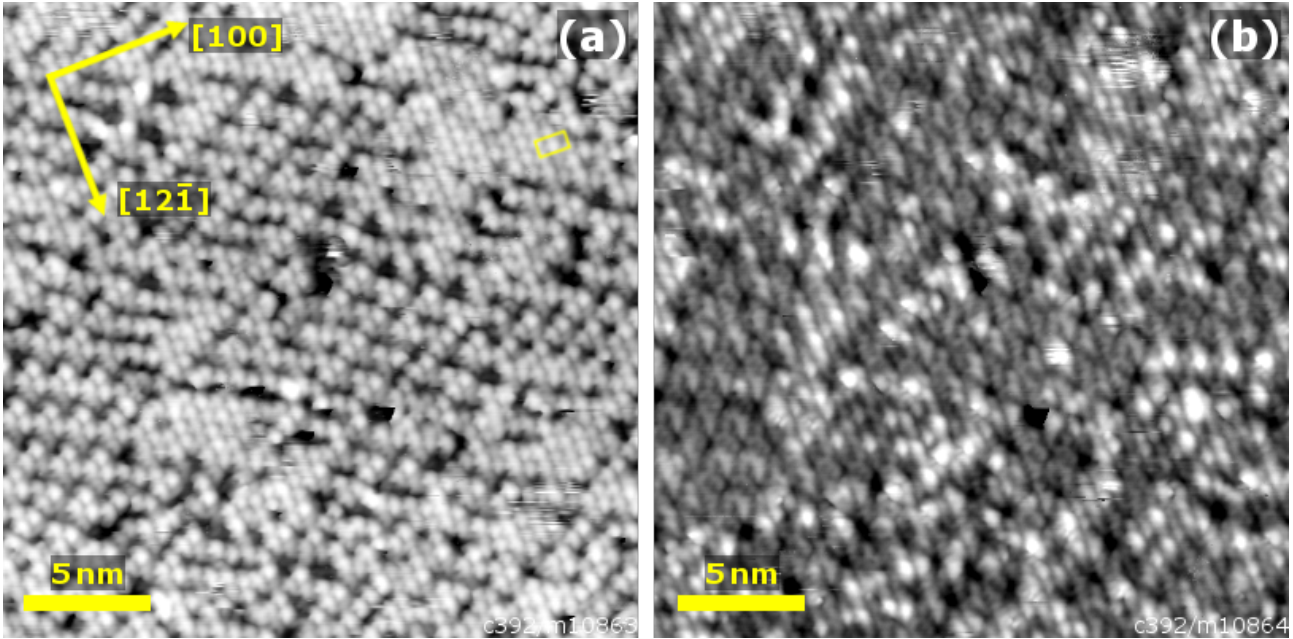


Figure 36: $25 \times 25 \text{ nm}^2$ STM images of the (2×1) $\alpha\text{-Fe}_2\text{O}_3(012)$ surface after dosing atomic hydrogen, then annealing in UHV (5 minutes at 150°C). (a) filled states image, $U = -1.2\text{V}$, $I = 0.1\text{nA}$. (b) empty states image, $U = +1.2\text{V}$, $I = 0.1\text{nA}$. Arrays of dark features are visible in both images, some of them in neither the $[12\bar{1}]$ line direction nor in one of the 60° domain directions.

was deposited. While the islands reproducibly appear after dosing Ti and annealing in UHV, no such features were ever observed on clean Fe_2O_3 .

The one-dimensional chains are shown more clearly in Fig. 38. They appear elevated in both positive and negative sample bias, but not as high as the islands. The single features that make up the chains could be the round features of the (2×1) surface, and they always appear along the 'narrow' trenches, but are drawn closer together than on the clean (2×1) surface.

4.8 Other results

To test reactivity to the residual gas, large amounts of CO were dosed on one of the samples at 300 K, which was studied in STM before and after dosing. No difference was observed, so there appears to be no reactivity of either surface to CO at room temperature.

In the same way described above for titanium, 0.1 monolayers of platinum were deposited on the clean (2×1) surface, as shown in Fig. 39. No ordering is observed directly after deposition, and after annealing to 200°C for 10 minutes, the adatoms arrange in large clusters, leaving clean surface around them.

As mentioned above, one aspect that had to be considered when working with hematite single crystals is conductivity. Slight charging effects were observed on all samples at all temperatures, and all samples had to be slightly reduced by sputtering and annealing in UHV to increase conductivity to a level sufficient for STM at room temperature. However, even after reduction, an unusual charging phenomenon was observed at low temperatures, which in the course of this work were only achieved in the MRS chamber, where only one of the samples was studied. Below 121 K, the XPS spectra changed significantly in shape and were shifted to much higher binding energies, as shown in Fig. 40. The O1s peak appears to be split into multiple separate features, with a different shape on the (2×1) termination than on the (1×1) surface. To confirm

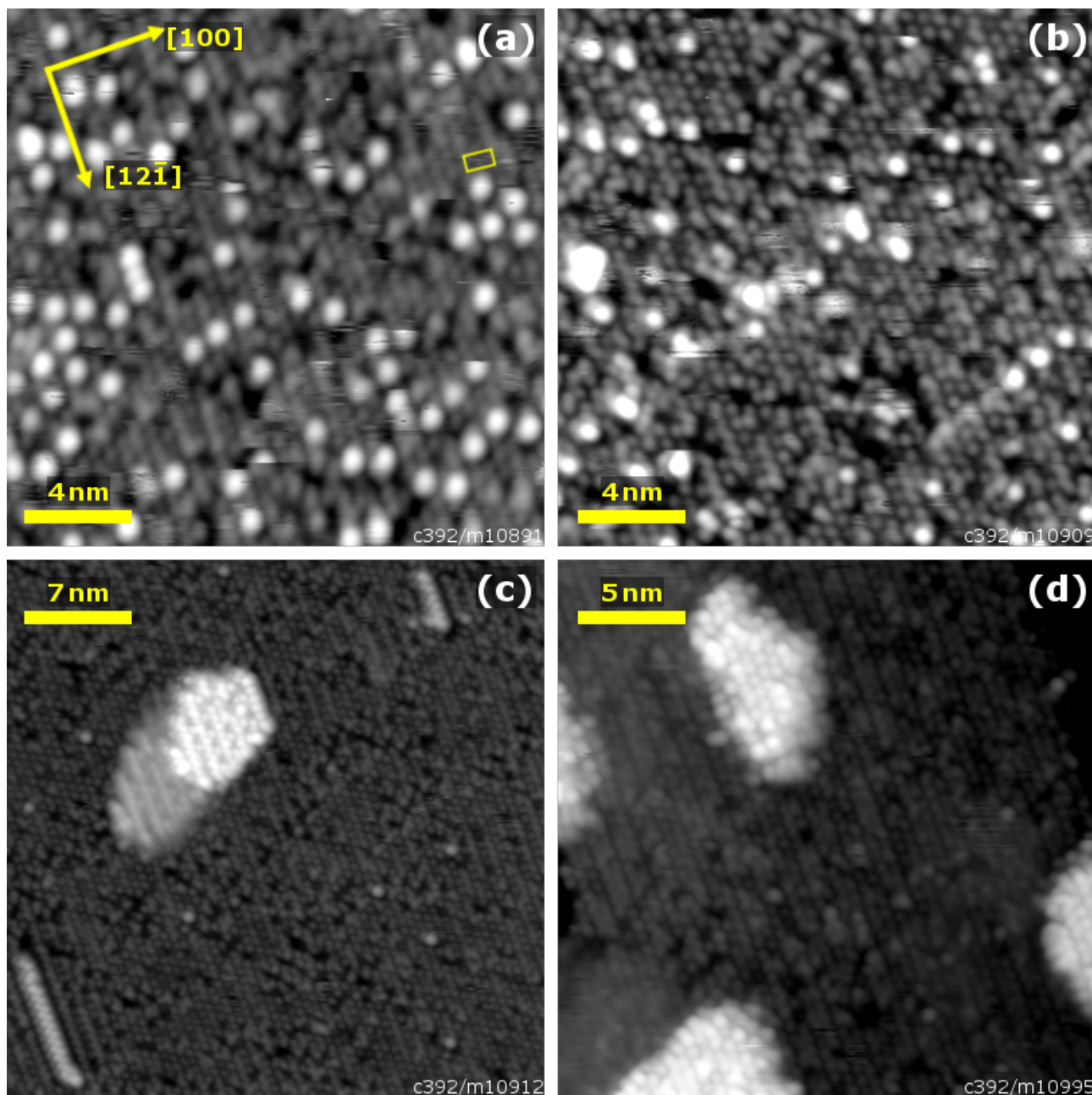


Figure 37: Filled states STM images of Ti adatoms on the $\alpha\text{-Fe}_2\text{O}_3(012)$ (2×1) surface. (a) 0.1 monolayers (ML) Ti as deposited on the (2×1) surface ($20\times 20\text{ nm}^2$, $U = -3\text{ V}$, $I = 0.1\text{ nA}$); (b) after 5 minutes annealing at 150°C ($20\times 20\text{ nm}^2$, $U = -2\text{ V}$, $I = 0.1\text{ nA}$); (c) after 5 minutes annealing at 200°C ($35\times 35\text{ nm}^2$, $U = -2\text{ V}$, $I = 0.1\text{ nA}$); 'shadow' on the left side of the island is due to a double tip; (d) after depositing 1 ML Ti on the clean surface and 10 minutes annealing at 200°C ($25\times 25\text{ nm}^2$, $U = -2\text{ V}$, $I = 0.1\text{ nA}$)

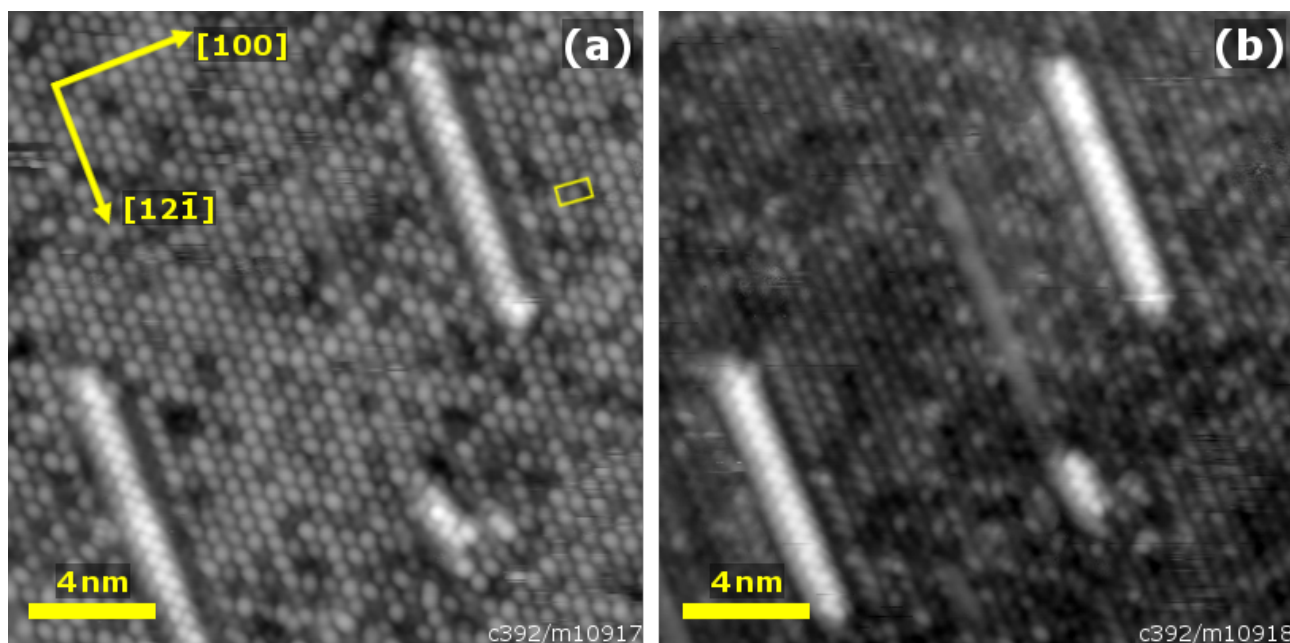


Figure 38: 20x20 nm² STM images of Ti adatoms on the α -Fe₂O₃(012) (2×1) surface, after depositing 0.1 monolayers Ti and annealing for 5 minutes at 150°C and 200°C each. (a) U = -1 V, I = 0.1 nA; (b) U = +1 V, I = 0.1 nA.

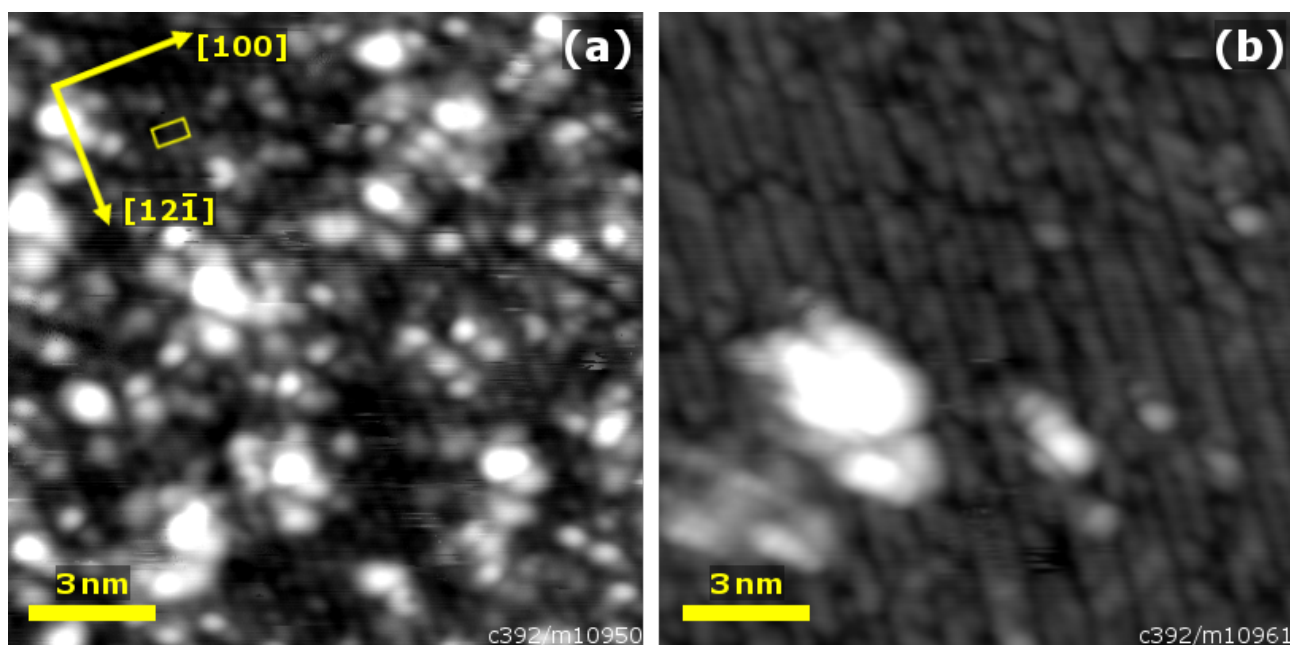


Figure 39: 15x15 nm² STM images of Pt adatoms on the α -Fe₂O₃(012) (2×1) surface (a) after depositing (U = +2 V, I = 0.1 nA); (b) after annealing for 10 minutes at 200°C (U = -2 V, I = 01 nA).

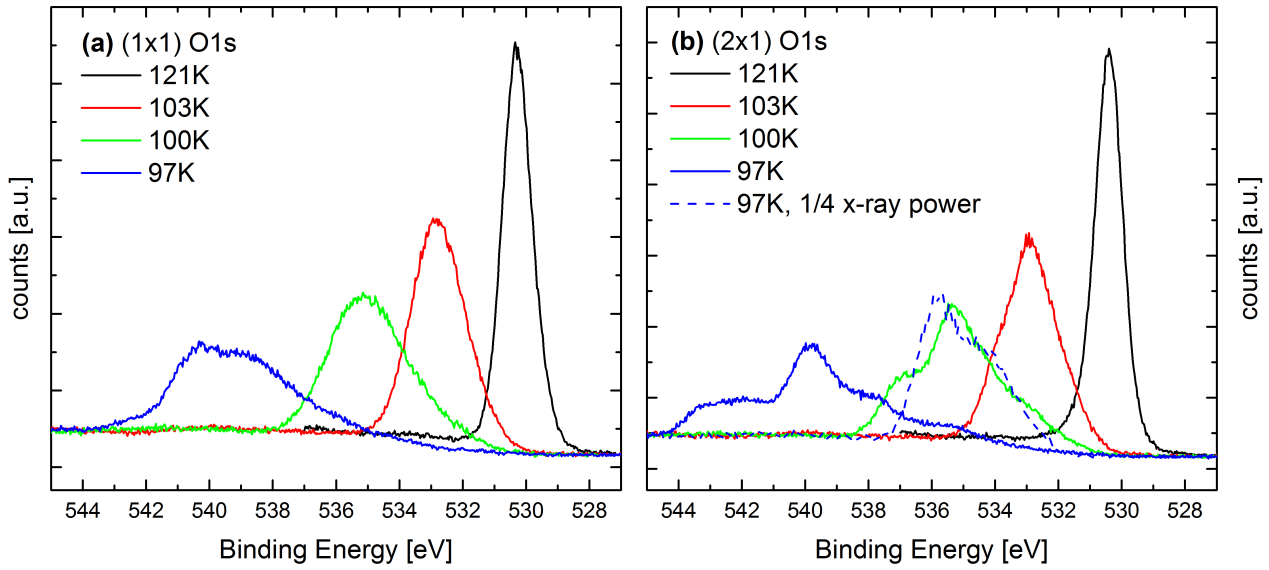


Figure 40: 75° grazing emission XPS spectra of the O1s region on both the (1×1) and the (2×1) surface at different temperatures. At 121 K and above, the main O1s peak is slightly shifted to higher binding energies compared to the literature value of 530.1 eV, but basically unchanged in shape. At low temperatures, the peak changes shape and drastically shifts to higher binding energies. All other peaks were also changed in a similar fashion.

that this was indeed a charging effect, XPS spectra were also taken at lower power of the x-ray source, shown in Fig. 40 (b), which resulted in a smaller peak shift. Both the (1×1) and the (2×1) surface exhibit peak shifts in the same order of magnitude, suggesting that reduction of the surface does not play a large role in this effect. However, since the other samples were not studied at low temperature to date, it remains to be seen if the transition temperature depends on other factors like the grade of reduction of the bulk, or if it is a characteristic property of hematite.

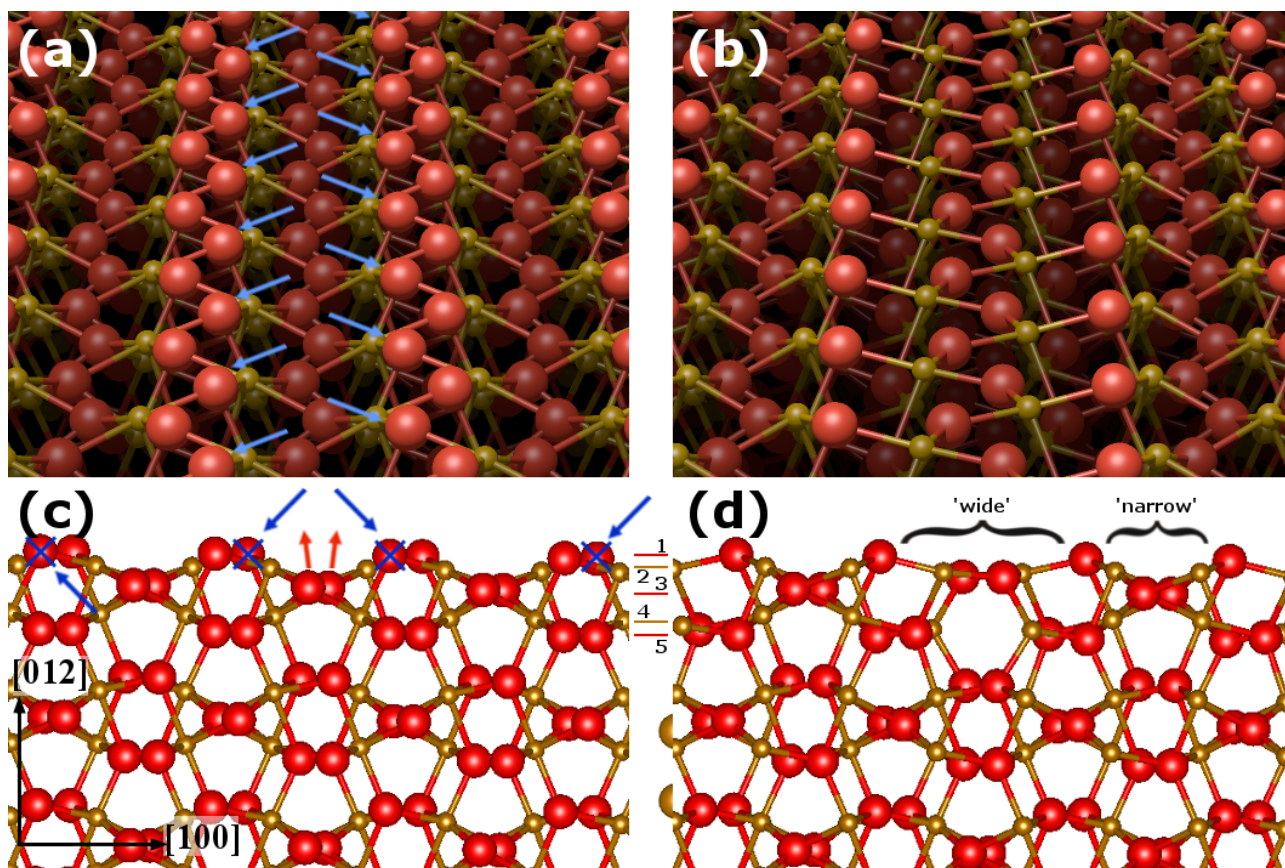


Figure 41: Perspective view (a,b) and side view (c,d) of the bulk-terminated (1×1) surface (a,c) and the proposed (2×1) surface (b,d) after relaxation via density functional theory; red: oxygen, golden: iron. The oxygen atoms that are removed to obtain the (2×1) surface are indicated by blue arrows and crosses in (a) and (c). Labelling of the first five layers is annotated in (c/d). Red arrows in (c) indicate the direction in which the layer 3 oxygen anions in the 'wide trenches' move during relaxation, breaking a bond with the layer 4 iron cations.

5 Discussion

5.1 The clean surfaces

All data presented here appears to support the model of a simple bulk truncated termination for the (1×1) surface. The STM images shown in Fig. 6 show zig-zag lines in both positive and negative bias, and the relative location of the defects visible in both images indicates that different species are imaged. As shown in Fig. 41 (a), both oxygen and iron are arranged in a zig-zag pattern on the surface. Density functional theory (DFT) calculations were contributed by Magdalena Bichler and Peter Blaha of the Institute of Materials Chemistry (TU Wien). These calculations allow relaxation of the surface structure to the energetically most favourable calculated atom positions, as well as determination of the density of states (DOS) of the separate ions and the total surface energy. The calculated DOS for the (1×1) surface is shown in Fig. 42 (a) and (b). Since iron states dominate above the Fermi level, and oxygen states are slightly stronger below the Fermi level, it is reasonable to assume that oxygen is imaged in negative bias STM, while iron is visible in the positive bias images. The defects in the (1×1) STM images might be molecular and dissociated water, which TPD in combination with XPS confirmed to be present as a mixed phase on the surface up to 375 K. Additionally, since the

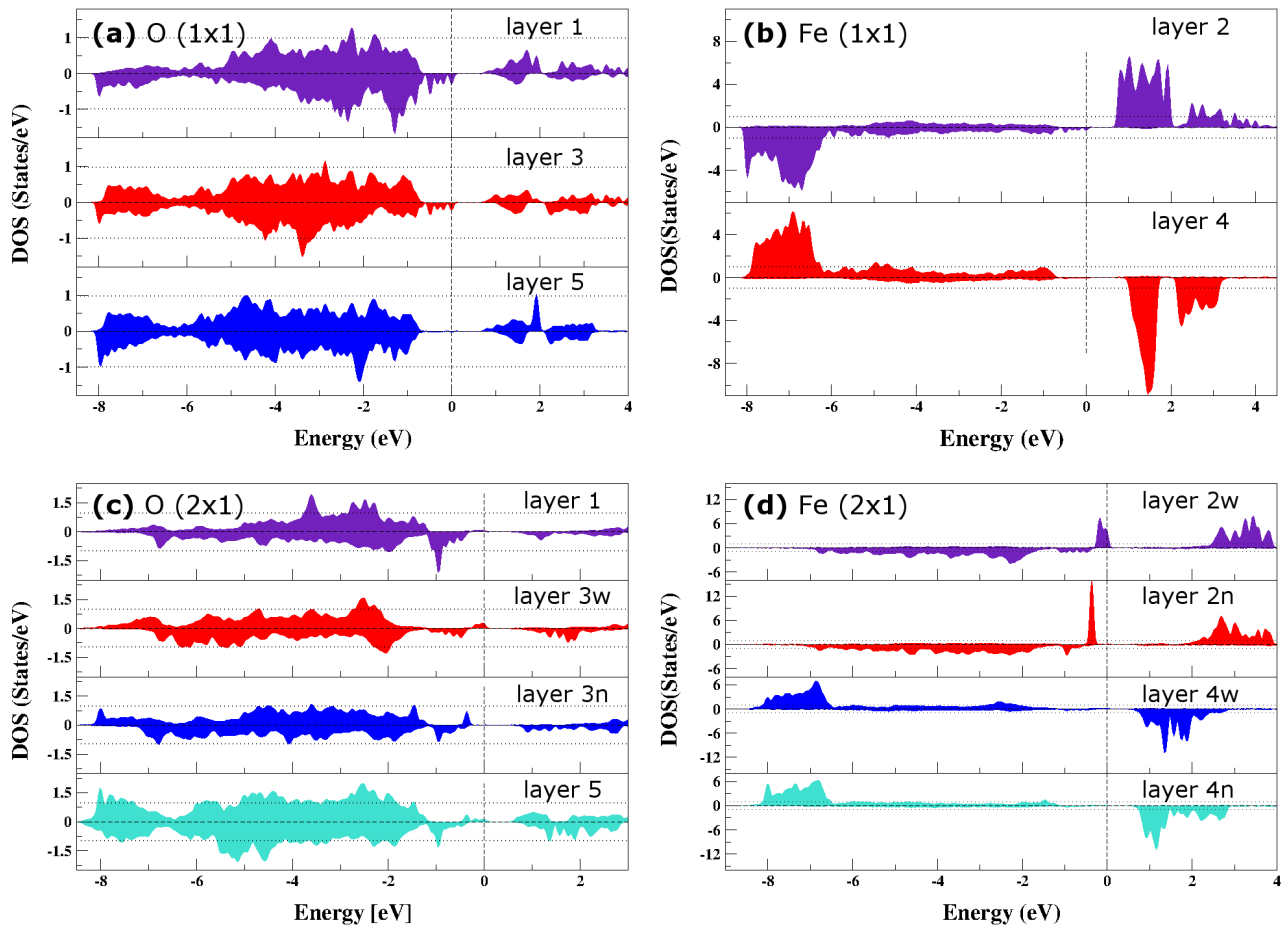


Figure 42: Calculated density of states for the bulk-terminated surface (a,b) and the alternating trenches (2 \times 1) reconstruction (c,d). Layers are numbered by their position in the bulk-terminated model, with a suffix to distinguish the atoms in wide or narrow trenches in the reconstructed surface (see Fig. 41). Data and images provided by Magdalena Bichler and Peter Blaha (Institute of Materials Chemistry, TU Wien), to be published.

sticking coefficient for water is extremely high on the (1×1) surface at low coverages even at room temperature, as shown in Fig. 23 (a), it is highly improbable to get an STM image of the (1×1) surface without any water on it at normal experiment conditions.

For the clean (2×1) surface, several models have previously been discussed. The reconstruction proposed by Gautier-Soyer et al. [22], which these authors say extends 25-30 Å into the bulk, was already in poor agreement with results published by Henderson [23–25, 31], and does not explain the $c(2\times 1)$ pattern observed in STM. Furthermore, comparison of normal and grazing emission XPS (Fig. 10) suggests that the Fe^{2+} created by reduction are concentrated at the surface; this would not be the case in the Gautier-Soyer model. Henderson et al. initially suggested a model in which every other oxygen atom in every other zig-zag row is missing [23], and later proposed a ridge/trough model in which every other oxygen zig-zag row is completely removed [24, 25, 31]. The latter model is in clear disagreement with the STM and AFM images shown in Figs. 7, 8 and 13, since no large-scale ridge/trough structure can be seen under any conditions. The less reduced model, based on removing one oxygen atom per (2×1) unit cell, cannot be dismissed completely based on the data shown here, but does not explain the $c(2\times 1)$ pattern observed in STM or the water adsorption behaviour.

Since previous models appear to be in poor agreement with the data collected here, a new model is proposed, in which every other oxygen atom is removed in every oxygen zig-zag row. By alternating between the left and right side of the zig-zag rows, as indicated by the blue arrows in Fig. 41, a (2×1) periodicity is obtained, with the remaining surface oxygen atoms arranged in a roughly $c(2\times 1)$ pattern. The atom positions in this model were optimized via DFT by Magdalena Bichler and Peter Blaha (Institute of Materials Chemistry, TU Wien). Relaxation is achieved by iteratively calculating the net forces on the structure and allowing the atoms to move until a local minimum is reached. The resulting 'relaxed' structure is shown in Fig. 41 (b) and (d). The iron cations in layer 2 (as labelled in Fig. 41) relax upwards into a fourfold coordinated position in the 'wide trenches', as do the wide trench oxygen atoms in layer 3 (indicated by the red arrow in Fig. 41 (c)), breaking bonds to layer 4, thus creating fourfold coordinated iron there as well. The layer 2 iron atoms in the 'narrow trenches' also achieve fourfold coordination, but stay in positions roughly equivalent to the (1×1) bulk terminated surface. Only the layer 4 wide trench iron cations end up in truly tetragonal coordination, while the fourfold coordinated layer 2 iron cations are close the topmost face of their respective tetrahedra. The calculated density of states is shown in Fig. 42 (c) and (d). Strong in-gap states are observed for the top layer iron cations, which qualitatively fits the UPS data shown in Fig. 11. The calculated charge in the narrow trenches is Fe^{2+} in layer 2, with bulk-like Fe^{3+} in layer 4. In the wide trenches, the additional charge is split between the layer 2 and layer 4 iron cations. This difference in charge might indicate different reactivity of the iron cations in the two trench types.

The same species, arranged in a $c(2\times 1)$ pattern, appears to be imaged in STM in both positive and negative bias (Figs. 7 and 8), and the lines in the $[12\bar{1}]$ direction appear paired under some, but not all, bias and tip conditions. The pairing can be explained by the proposed model as a difference in the narrow and the wide trenches, while the topmost oxygen atoms form a roughly $c(2\times 1)$ pattern, although the 'center' atom is slightly offset in the $[100]$ direction. However, this offset can be explained if the features imaged in STM are not solely the oxygen atoms, but a combination of the layer 1 oxygen anions and their two neighbouring layer 2 iron cations, since the position of the spots in STM corresponds roughly to the center of mass of these three atoms, shown as green circles in Fig. 43 (c). This would also explain the AFM image shown in the inset to Fig. 13 (b), where the $c(2\times 1)$ features are arranged in the same fashion as in the STM images, but with an elongated shape instead of round.

The proposed model can be reconciled with the STM images shown in Figs. 7, 8 and 9, as well as with the XPS data shown in Fig. 10. Assuming that the dark features in the AFM images shown in Fig. 13 are iron, the observed phase shift in the $[12\bar{1}]$ direction in Fig. 13 (b) is also in good agreement with the calculated positions of the layer 2 iron cations in the relaxed (2×1) surface. Finally, preliminary DFT results show that the proposed (2×1) reconstruction is the most stable surface termination at low oxygen chemical potential among several ones that were tested, including all previously proposed models, while the (1×1) bulk terminated surface is the most stable one in oxidizing conditions. However, another possibility based on sub-surface iron interstitials is being explored at this time, and it remains to be seen if that model would yield even better results.

5.2 Surface interaction with water

Imaging water adsorption on the (1×1) surface at room temperature was challenging, and the few images that could be obtained are not easy to interpret, such as the one shown in Fig. 14. Several distinct species appear to be resolved, which is not surprising considering the XPS spectra of the O1s region after dosing water (Fig. 24), which exhibit both molecular and dissociated water peaks even at room temperature. One would expect one type of feature each for molecular water, terminal and bridging hydroxyls, as well as some possible combinations of the three. Interpretation of the STM features seems premature at this point, except that all species not aggregated in clusters appear to be extremely mobile at room temperature, and that Fig. 14 does not show a full coverage. Judging by the comparison of peak areas after dosing at 100 K and at 300 K (Fig. 20), it appears that a monolayer of water can not be saturated at room temperature on the (1×1) surface. However, the 340 K TPD peak exhibits first-order line shape, which is characteristic of unimolecular, as opposed to recombinative, desorption. Henderson explained this behaviour by strong pairing of the terminal and bridging hydroxyls through hydrogen-bonding interactions [23]. The high temperature tail of the TPD peak corresponds to dissociated water according to XPS (Fig. 24 (b)), and is saturated first, which can be explained as surface defect sites stabilizing some hydroxyls.

The capacity for water on the (1×1) surface is only ≈ 1.52 molecules per unit cell for the 340 K peak, which is surprising considering that two pairs of under-coordinated iron and oxygen are available per unit cell. Since both sites should in theory be equivalent, the lower than expected capacity might point to steric hindrance. At room temperature, saturation capacity is even lower, with only ≈ 1.07 molecules per unit cell. However, considering that 300 K is already well into the leading edge of the 340 K desorption peak, this is perhaps not surprising.

On the (2×1) termination, water again forms a mixed phase of dissociated and molecular species when dosed at 100 K, but is dissociated completely when dosed at 300 K. When water is dosed at 100 K, heated to 300 K and then cooled back down, as shown in Fig. 29, both desorption and dissociation of previously molecular water appear to occur, depending on coverage (Fig. 29), again yielding only dissociated water. In STM, two different phases are observed depending on coverage. At first, water arranges in a 'domained' overlayer, manifesting in negative bias imaging as blacked out lines of $c(2\times 1)$ features in 60° angles to the $[12\bar{1}]$ direction, and in positive bias as one large plus one neighbouring smaller spot (Figs. 15, 16, 17 and 18). It should be mentioned that the boundaries of these domains can be observed to shift, and interphase domain boundaries along the domain directions are common, which excludes intrinsic properties of the underlying surface as the source of the domain ordering.

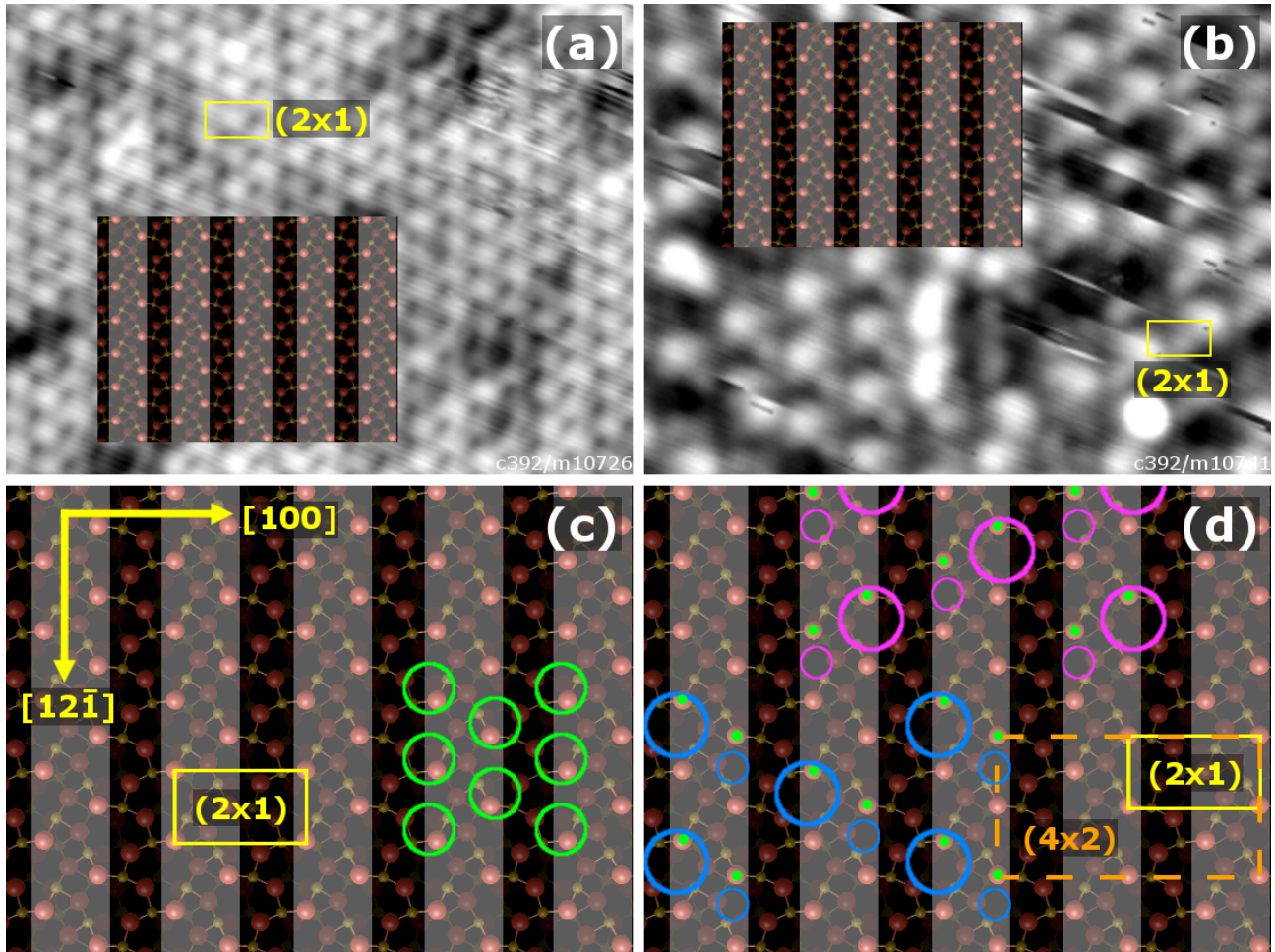


Figure 43: (a) Detail of a negative bias STM image of the clean (2×1) surface already shown in Fig. 8, with an inset showing a top view of the proposed model for the (2×1) surface, where the 'narrow', (1×1) -like trenches are marked in white and aligned with their assumed positions in the STM image. (b) Detail of the positive bias STM image with water on the (2×1) surface already shown in Fig. 15, with the same inset as in (a). Large and small features are observed each on one side of the trenches; which feature is on which side varies by domain direction. (c) Top view shown as an inset in (a) and (b), with the green circles marking the features imaged in STM on the clean (2×1) surface, such as in (a). (d) Top view with one possible position for the adsorbate features in (b) marked with blue circles for one domain direction and magenta circles for the other. Assuming the circles mark OH^- positions, corresponding H^+ adsorption sites are marked with green dots. Oxygen is red and iron is golden in all four images.

Details of the STM images shown in Figs. 8 and 15, and how they relate to the proposed model, are shown in Fig. 43. To describe the adsorbate positions, a (4×2) supercell has to be considered instead of the simple (2×1) unit cell, as shown in Fig. 43 (d). One large type of feature stands out in Fig. 43 (b), positioned either on the left or on the right side of the 'narrow', (1×1) -like trenches, with a density of two features per (4×2) unit cells, which corresponds to only 0.5 features per (2×1) unit cell. However, an additional smaller feature can be seen for every large one. This combination of two visible spots could be interpreted either as a terminal and a surface hydroxyl, which would mean that we observe only half a dissociated water molecule per (2×1) unit cell; or both spots might correspond to terminal OH in structurally different sites, with the remaining hydrogen atoms not visible in STM. This would yield one dissociated water molecule per (2×1) unit cell. Since TPD seems to support the latter interpretation, with the 'domains' interpreted as half coverage, possible positions for four hydroxyls per (4×2) supercell are considered in Fig. 43 (d). The large and small circles correspond to the two different types of site, while the two possible domain directions are distinguished by colour. Judging from the relative positions of large and small spots in the STM image shown in Fig. 43 (b), it would seem that one of the sites, here assumed to be the large features in STM, is bridging two iron cations, one of them in the 'wide' trench. This would result in the second OH^- , marked by the small circles in Fig. 43 (d), positioned close to a 'narrow' trench iron cation, perhaps bridging to the surface hydroxyl along the $[12\bar{1}]$ direction. A reason for this different type of adsorption site might be an asymmetric surface distortion that is energetically more favourable than a symmetric one. Corresponding adsorption sites for the remaining hydrogen are marked in green in Fig. 43, assuming strong pairing of OH^- and H^+ . Looking back at the negative bias STM images of the domained structure, as shown in Fig. 15 (a), the resulting pattern of surface hydroxyls would actually fit nicely to the features blacked out by the adsorbates. Two different types of adsorption site might also explain the patterns of brighter and darker features along the blacked out lines, as seen in Figs. 16 and 17. If the 'domained' structure is instead interpreted as only 0.5 dissociated H_2O molecules per (2×1) unit cells, the large and small circles could instead be interpreted as surface and terminal hydroxyl sites, respectively, but as mentioned above, this density of adsorbates does not appear to match the TPD results.

Interestingly, the TPD spectra obtained for water on the (2×1) surface are influenced by the adsorption temperature. At room temperature, the behaviour can be separated into two coverage regimes. For initial coverages between 0.1 and 1 D_2O molecule per (2×1) unit cell (Fig. 27), the TPD curves exhibit aligned leading edges, characteristic of zero-order desorption. Such behaviour suggests that the OH and H species are not spatially separated on the surface, and Henderson has previously proposed that preferential desorption from the ends of one-dimensional arrays can account for the lack of coverage dependence [23]. Obtained STM images of a partially desorbed 'domained' superstructure, which exhibit islands of domains and clean surface, are consistent with this interpretation.

Once the domains are saturated at one molecule per unit cell, the sticking coefficient drops (Fig. 23 (b)), and the leading edges of the TPD peak shift toward higher temperature with increasing coverage. We attribute the change to the nucleation and growth of the 'zig-zag phase', as observed in STM in Fig. 18. Interestingly, the peak retains a pseudo-zero-order line shape, suggesting that desorption from the ends of the zig-zag rows may be rate limiting.

Comparison of the TPD peak areas in Fig. 27 yields ≈ 1.09 molecules per (2×1) unit cell for what is assumed to be the domained phase, but only ≈ 1.73 molecules per (2×1) unit cell for what is here considered saturation coverage at room temperature, as discussed above. This

might mean that saturation was not quite reached with the 8.0 L nominal dose, that some areas are not accessible for two molecules per unit cell due to steps or defects, or that some partial desorption occurs before the TPD measurements. It is however worth reiterating that no molecular water was observed in XPS at any coverage at room temperature, which appears to exclude areas of (1×1) terminated surface from the list of possible deficiencies.

When dosing a saturation coverage of water on the (2×1) surface at room temperature and then desorbing part of it, as shown in Fig. 28, the resulting TPD peak keeps the characteristics of the saturation phase, suggesting that once it is formed, the bold zig-zagging structure does not go back to the domained phase. On the other hand, since the saturation phase is never found until the domained structure is almost saturated, it is not entirely clear which one is actually the energetically favourable phase, only that a large energy barrier can be expected for transformation between them. When dosing more water on a preheated surface, which should consist of clean (2×1) terminated areas and areas with saturation water coverage, a left flank probably corresponding to a domained superstructure forming on the clean areas is observed in TPD, but the saturation coverage peak also grows strongly, as shown in Fig. 28 (c). This suggests that formation of the zig-zagging saturation phase is forbidden or very unlikely at low coverages, but once some areas of saturation coverage have been formed, they can be expanded even though clean surface sites would also be available. This might be due to a large surface distortion to accommodate the zig-zags that is only stable above some threshold size.

The low temperature behaviour of water on the (2×1) surface appears to be more complicated than the one observed when dosing at 300 K. The XPS spectra of the O1s region shown in Fig. 29 (a) exhibit clear features for both molecular and dissociated water at all coverages, which means that even the monolayer peak at above 300 K is not initially dissociated after dosing. As discussed above, the TPD peaks shown in Fig. 25 at first grow in a similar fashion to the ones for room temperature doses, but around the point where the 395 K peak saturates and a lower temperature feature starts growing in, the monolayer peak starts broadening. This might be explained by the low temperature peak hindering dissociation of the molecular water, but the fact that a slower heating rate, as shown in Fig. 26, does not change the high coverage curves in any significant way, is puzzling in this context. Further examination of higher water coverages, especially with imaging techniques, will be required. However, when dosing at low temperature, comparison of the TPD peak area of the monolayer peak at 'domained' coverage (before leading edges start shifting) and at saturation coverage (at maximum peak height, before the low temperature peak starts growing in) matches the expected one and two molecules per unit cell respectively rather well, which is not the case when dosing at room temperature. As to the sites of water on the (2×1) surface, Henderson concluded from HREELS that terminal OH would probably be found in structurally (1×1) -like sites [23]. This is in good agreement with positive bias STM images like the one shown in Fig. 15, which show that the adsorbates are found exclusively along the 'narrow trenches', which are (1×1) -like in the proposed model for the (2×1) reconstruction.

Comparing the TPD peak areas of D_2O on $\alpha\text{-Fe}_2\text{O}_3(012)$ at low temperatures (Figs. 20 and 25), the total capacity for water, excluding multilayer adsorption, appears to be roughly the same for both surfaces. The monolayer peak saturates at ≈ 1.52 molecules per (1×1) unit cell for the (1×1) terminated surface, and at ≈ 1.75 molecules per (2×1) unit cell for the (2×1) terminated surface, when dosing at 100 K. This would mean that the surface density of D_2O on the (2×1) surface is roughly 58% of that on the (1×1) for the highest temperature peaks, which happens to be the only features above room temperature on both surfaces. However,

when dosing at room temperature (Figs. 20 and 27), the (1×1) surface saturates at ≈ 1.07 D_2O molecules per (1×1) unit cell, while the (2×1) surface can bind ≈ 1.73 molecules per (2×1) unit cell, which corresponds to 81% of the molecule density on the (1×1) surface. Finally, comparing the O1s region of the XPS spectra of both surfaces at room temperature, as shown in Fig. 30, leads to the conclusion that both surfaces dissociate roughly the same amount of water, but that some additional molecular water is present on the (1×1) surface. Comparison of the XPS peak areas yields an estimate of 63% dissociated water, which is reasonably close to the 75% predicted by Rustad et al. [38] with a parameterized classical potential model.

After liquid water drop experiments, no molecular water was observed in XPS, as shown in Fig. 31. While this might theoretically point to a difference between the surface interaction with gaseous and with liquid water for the (1×1) termination, it is also easily explained by insufficient XPS sensitivity, as discussed in chapter 4.4. However, it would be premature to rule out a difference in reactivity based on this data. Further research is required.

5.3 Preliminary data

The oxygen TPD spectra shown in Figs. 33 and 34 are different from the ones published previously [31] in that oxygen was not previously dosed below 120 K, and physisorption only starts below 80 K. The reactivity of the (1×1) surface does not appear to hold any surprises, but the (2×1) surface shows some transformation after first dosing oxygen at low temperatures and heating. This effect was not observed when dosing at 100 K, so physisorbed oxygen appears to be a precondition for the process to occur, which is probably why it was not reported by Henderson [31]. Since the (2×1) surface does not seem to get transformed back to (1×1) , one possible explanation might be that physisorbed O_2 molecules are bound to oxygen vacancy defect sites at the surface. In the 260 K desorption feature, these molecules could then either heal the defects or change them in some way that prevents readsorption during later cycles. Labelling the surface with ^{18}O or dosing ^{18}O on a normally prepared surface might provide further insights.

Studying the STM images taken while dosing oxygen (Fig. 32), something is obviously adsorbing on the surface, but according to TPD, no oxygen should be able to bind to the clean surface at this temperature. However, one has to consider that there was also some water adsorbing on the (2×1) surface during the STM experiments, with some hydroxyls already present before starting to dose oxygen, which was probably not the case in the TPD experiments due to much better background pressure. Henderson notes that oxygen is stabilized by the coadsorption of water [31], so it seems reasonable to assume that the species observed in Fig. 32 that look like the typical adsorbed water features are just that, and that the oxygen adsorption features are actually the bright spots in Fig. 32 (c) and (d), as well as some part of the disordered areas in Fig. 32 (e) and (f). A next step towards understanding these images would be reproducing this coadsorption in TPD experiments, or dosing water and oxygen in more controlled amounts before STM measurements.

The atomic hydrogen data presented in chapter 4.6 is hard to interpret due to the lack of information about how much hydrogen was dosed, and what other species might have been adsorbed while dosing hydrogen. However, STM images like the one shown in Fig. 35 (a) exhibit zig-zagging features that resemble full water coverage, but not only in large patches but also as pairs and triplets, and next to clean-looking surface areas, which usually prevent the saturation water phase from forming. If the previous assumption holds that the saturation water coverage

is connected to severe distortions of the surface, adsorbed atomic hydrogen without terminal OH might result in similar looking features without distorting the surface, thus not requiring large areas to be stable. This would imply that the bold zig-zagging lines seen in the saturation water coverage STM images show surface hydroxyls adsorbed on layer 1 oxygen anions.

The severely changed surface after adsorbing hydrogen and then annealing at 150°C, shown in Fig. 36, might result from two hydrogen atoms taking one oxygen from the surface to desorb as H₂O, leaving behind oxygen vacancies.

The experiments with titanium are especially interesting because Ti is often used as a dopant to improve conductivity in Fe₂O₃ PEC cells, and because iron and titanium oxides form a complex containing several mixed materials such as ilmenite and pseudo-brookite [33], some of which might potentially also be of interest for solar water splitting [39]. Immediately after depositing titanium on the α -Fe₂O₃(012) (2×1) surface, the adatoms appear to arrange in a periodic pattern, perhaps diffusing to one preferential position per (2×1) unit cell. After annealing to 200°C, islands grow on the surface, and one-dimensional chains are observed (Figs. 37 and 38). The islands, which appear to have the same structure as the underlying hematite surface, might be interpreted as some mixed oxide isostructural to Fe₂O₃ with high titanium content, such as ilmenite (FeTiO₃), segregating at the surface, although this begs the question where the additional oxygen would come from.

No simple explanation can be given for the one-dimensional chain structures at this point, but since they appear as a slightly distorted, brighter continuation of the clean surface STM features, some spatial distortion or electronic effect due to titanium incorporation in the narrow trenches might conceivably play a role.

Finally, the low temperature charging effect shown in Fig. 40 is unexpected, and hard to interpret with the data available at this point. As discussed above, it remains to be seen if the transition temperature is intrinsic to hematite or depends on sample history. Macroscopic temperature-dependent conductivity measurements might shed more light on the transition behaviour, which appears rather sharp based on the XPS data.

6 Summary and Outlook

Bulk samples of α -Fe₂O₃(012) could reproducibly be prepared with sufficient conductivity for STM measurements. The previous assumption that the (1×1) surface is bulk terminated is supported by all LEED, STM and XPS data obtained in the course of this work. However, previously discussed models for the reduced (2×1) surface do not offer satisfactory explanations for the STM images shown in Figs. 7, 8 and 9. A new model, introduced in Fig. 41, is therefore proposed for the (2×1) termination. This model is in good agreement with all previously described experiments, as well as with the data presented in this thesis, and is supported by preliminary DFT results as the most stable surface at reducing conditions.

The reactivity of both α -Fe₂O₃(012) terminations with water were studied in depth with STM, XPS and TPD. STM images of H₂O on the (1×1) surface are ambiguous, and further research is needed to determine its atomic scale coordination, but XPS reveals a mixed phase of molecular and dissociated water at all coverages, with 63% dissociated at room temperature and saturation coverage.

Water on the (2×1) surface was shown to be entirely dissociated at room temperature, with some molecular water present at low temperatures. Two distinct, not previously described phases were observed in STM, and could be associated with a change in the behaviour of the TPD monolayer peak at half coverage. An atomic-scale description of these phases remains to be found. Experiments with liquid water drops were attempted, but not yet successful.

Preliminary data was obtained for O₂ adsorption on the α -Fe₂O₃(012) surface, as well as for surface interaction with atomic hydrogen and with titanium and platinum adatoms. The O₂ TPD data presented here expands on previously published results, and reveals transformation of the (2×1) surface after heating with physisorbed O₂, the effects of which remain to be examined. Co-adsorption of O₂ with water was observed on the (2×1) surface, but not expanded on thus far. Results from atomic hydrogen experiments are at this point hard to put into context, but might help with interpretation of water dissociation on the (2×1) surface. Apart from clustering at 200°C, no interesting behaviour was observed for platinum adatoms, but depositing titanium and annealing yields two types of ordered structures, shown in Figs. 37 and 38. Further investigation of incorporation or segregation of titanium on hematite might provide insights into the mechanisms behind improved photocatalytic activity of Ti-doped Fe₂O₃.

An unexpected change in XPS spectra was observed at temperatures below 121 K, which is attributed to a sharp drop in conductivity at that point. Further investigation of this phenomenon is required, as well as a theoretical explanation.

The results presented in this thesis highlight the complexity of dissociation processes on the α -Fe₂O₃(012) surface. Understanding the exact atomic configuration of the (1×1) and (2×1) terminations and their interaction with water will be the groundwork for an evidence-based approach to improving the photocatalytic properties of hematite.

References

- [1] K. Sivula, F. Le Formal, and M. Grätzel, “Solar water splitting: progress using hematite (α - Fe_2O_3) photoelectrodes,” *ChemSusChem*, vol. 4, no. 4, pp. 432–449, 2011.
- [2] A. G. Tamirat, J. Rick, A. A. Dubale, W.-N. Su, and B.-J. Hwang, “Using hematite for photoelectrochemical water splitting: a review of current progress and challenges,” *Nanoscale Horizons*, 2016.
- [3] L. A. Marusak, R. Messier, and W. B. White, “Optical absorption spectrum of hematite, α - Fe_2O_3 near IR to UV,” *Journal of Physics and Chemistry of Solids*, vol. 41, no. 9, pp. 981–984, 1980.
- [4] N. J. Cherepy, D. B. Liston, J. A. Lovejoy, H. Deng, and J. Z. Zhang, “Ultrafast studies of photoexcited electron dynamics in γ - and α - Fe_2O_3 semiconductor nanoparticles,” *The Journal of Physical Chemistry B*, vol. 102, no. 5, pp. 770–776, 1998.
- [5] J. Launay and G. Horowitz, “Crystal growth and photoelectrochemical study of Zr-doped α - Fe_2O_3 single crystal,” *Journal of Crystal Growth*, vol. 57, no. 1, pp. 118–124, 1982.
- [6] B. Warnes, F. Aplan, and G. Simkovich, “Electrical conductivity and Seebeck voltage of Fe_2O_3 , pure and doped, as a function of temperature and oxygen pressure,” *Solid State Ionics*, vol. 12, pp. 271–276, 1984.
- [7] B. Klahr, S. Gimenez, F. Fabregat-Santiago, J. Bisquert, and T. W. Hamann, “Electrochemical and photoelectrochemical investigation of water oxidation with hematite electrodes,” *Energy & Environmental Science*, vol. 5, no. 6, pp. 7626–7636, 2012.
- [8] B. Klahr, S. Gimenez, F. Fabregat-Santiago, T. Hamann, and J. Bisquert, “Water oxidation at hematite photoelectrodes: the role of surface states,” *Journal of the American Chemical Society*, vol. 134, no. 9, pp. 4294–4302, 2012.
- [9] M. Rioult, D. Stanescu, E. Fonda, A. Barbier, and H. Magnan, “Oxygen Vacancies Engineering of Iron Oxides Films for Solar Water Splitting,” *The Journal of Physical Chemistry C*, vol. 120, no. 14, pp. 7482–7490, 2016.
- [10] H. Magnan, D. Stanescu, M. Rioult, E. Fonda, and A. Barbier, “Enhanced photoanode properties of epitaxial Ti doped α - Fe_2O_3 (0001) thin films,” *Applied Physics Letters*, vol. 101, no. 13, p. 133908, 2012.
- [11] M. Rioult, R. Belkhou, H. Magnan, D. Stanescu, S. Stanescu, F. Maccherozzi, C. Rountree, and A. Barbier, “Local electronic structure and photoelectrochemical activity of partial chemically etched Ti-doped hematite,” *Surface Science*, vol. 641, pp. 310–313, 2015.
- [12] D. P. Woodruff, “Quantitative structural studies of corundum and rocksalt oxide surfaces,” *Chemical reviews*, vol. 113, no. 6, pp. 3863–3886, 2013.
- [13] H. Kuhlenbeck, S. Shaikhutdinov, and H.-J. Freund, “Well-ordered transition metal oxide layers in model catalysis—A series of case studies,” *Chemical reviews*, vol. 113, no. 6, pp. 3986–4034, 2013.
- [14] G. S. Parkinson, “Iron oxide surfaces,” *Surface Science Reports*, vol. 71, no. 1, pp. 272–365, 2016.

- [15] N. Condon, F. Leibsle, A. Lennie, P. Murray, D. Vaughan, and G. Thornton, "Biphase ordering of iron oxide surfaces," *Physical Review Letters*, vol. 75, no. 10, p. 1961, 1995.
- [16] C. H. Lanier, A. N. Chiaramonti, L. D. Marks, and K. R. Poeppelmeier, "The Fe_3O_4 origin of the 'biphase' reconstruction on $\alpha\text{-Fe}_2\text{O}_3$ (0001)," *Surface Science*, vol. 603, no. 16, pp. 2574–2579, 2009.
- [17] T. Nakau, "Electrical conductivity of $\alpha\text{-Fe}_2\text{O}_3$," *Journal of the Physical Society of Japan*, vol. 15, no. 4, pp. 727–727, 1960.
- [18] D. Benjelloun, J.-P. Bonnet, J.-P. Doumerc, J.-C. Launay, M. Onillon, and P. Hagemuller, "Anisotropie des proprietes electriques de l'oxyde de fer Fe_2O_3 α ," *Materials chemistry and physics*, vol. 10, no. 6, pp. 503–518, 1984.
- [19] G. Ketteler, W. Weiss, W. Ranke, and R. Schlögl, "Bulk and surface phases of iron oxides in an oxygen and water atmosphere at low pressure," *Physical Chemistry Chemical Physics*, vol. 3, no. 6, pp. 1114–1122, 2001.
- [20] W. Weiss and W. Ranke, "Surface chemistry and catalysis on well-defined epitaxial iron-oxide layers," *Progress in Surface Science*, vol. 70, no. 1, pp. 1–151, 2002.
- [21] R. J. Lad and V. E. Henrich, "Structure of $\alpha\text{-Fe}_2\text{O}_3$ single crystal surfaces following Ar^+ ion bombardment and annealing in O_2 ," *Surface Science*, vol. 193, no. 1, pp. 81–93, 1988.
- [22] M. Gautier-Soyer, M. Pollak, M. Henriot, and M. Guittet, "The (1×2) reconstruction of the $\alpha\text{-Fe}_2\text{O}_3$ ($\bar{1}012$) surface," *Surface science*, vol. 352, pp. 112–116, 1996.
- [23] M. A. Henderson, S. A. Joyce, and J. R. Rustad, "Interaction of water with the (1×1) and (2×1) surfaces of $\alpha\text{-Fe}_2\text{O}_3(012)$," *Surface Science*, vol. 417, no. 1, pp. 66–81, 1998.
- [24] M. A. Henderson, "Insights into the (1×1) -to- (2×1) phase transition of the $\alpha\text{-Fe}_2\text{O}_3(012)$ surface using EELS, LEED and water TPD," *Surface science*, vol. 515, no. 1, pp. 253–262, 2002.
- [25] M. A. Henderson, "Surface stabilization of organics on hematite by conversion from terminal to bridging adsorption structures," *Geochimica et cosmochimica acta*, vol. 67, no. 5, pp. 1055–1063, 2003.
- [26] J. Wang and J. R. Rustad, "A simple model for the effect of hydration on the distribution of ferrous iron at reduced hematite (012) surfaces," *Geochimica et cosmochimica acta*, vol. 70, no. 21, pp. 5285–5292, 2006.
- [27] C. S. Lo, K. S. Tanwar, A. M. Chaka, and T. P. Trainor, "Density functional theory study of the clean and hydrated hematite $(1\bar{1}02)$ surfaces," *Physical Review B*, vol. 75, no. 7, p. 075425, 2007.
- [28] K. S. Tanwar, J. G. Catalano, S. C. Petitto, S. K. Ghose, P. J. Eng, and T. P. Trainor, "Hydrated $\alpha\text{-Fe}_2\text{O}_3$ surface structure: Role of surface preparation," *Surface science*, vol. 601, no. 12, pp. L59–L64, 2007.
- [29] K. S. Tanwar, C. S. Lo, P. J. Eng, J. G. Catalano, D. A. Walko, G. E. Brown, G. A. Waychunas, A. M. Chaka, and T. P. Trainor, "Surface diffraction study of the hydrated hematite surface," *Surface Science*, vol. 601, no. 2, pp. 460–474, 2007.

- [30] S. Yin and D. E. Ellis, "DFT studies of Cr(VI) complex adsorption on hydroxylated hematite ($1\bar{1}02$) surfaces," *Surface Science*, vol. 603, no. 4, pp. 736–746, 2009.
- [31] M. A. Henderson, "Low temperature oxidation of Fe^{2+} surface sites on the (2×1) reconstructed surface of $\alpha\text{-Fe}_2\text{O}_3(01\bar{1}2)$," *Surface Science*, vol. 604, no. 13, pp. 1197–1201, 2010.
- [32] H. Guo and A. S. Barnard, "Thermodynamic modelling of nanomorphologies of hematite and goethite," *Journal of Materials Chemistry*, vol. 21, no. 31, pp. 11566–11577, 2011.
- [33] R. M. Cornell and U. Schwertmann, *The iron oxides: structure, properties, reactions, occurrences and uses*. John Wiley & Sons, 2003.
- [34] P. Tasker, "The stability of ionic crystal surfaces," *Journal of Physics C: Solid State Physics*, vol. 12, no. 22, p. 4977, 1979.
- [35] A. Grosvenor, B. Kobe, M. Biesinger, and N. McIntyre, "Investigation of multiplet splitting of Fe 2p XPS spectra and bonding in iron compounds," *Surface and Interface Analysis*, vol. 36, no. 12, pp. 1564–1574, 2004.
- [36] J. Pavelec, J. Hulva, D. Halwidl, R. Bliem, O. Gamba, Z. Jakub, F. Brunbauer, M. Schmid, U. Diebold, and G. S. Parkinson, "A multi-technique study of CO_2 adsorption on Fe_3O_4 magnetite," *The Journal of Chemical Physics*, vol. 146, no. 1, p. 014701, 2017.
- [37] W. Jitschin, M. Ronzheimer, and S. Khodabakhshi, "Gas flow measurement by means of orifices and Venturi tubes," *Vacuum*, vol. 53, no. 1-2, pp. 181–185, 1999.
- [38] J. R. Rustad, E. Wasserman, and A. R. Felmy, "Molecular modeling of the surface charging of hematite: II. Optimal proton distribution and simulation of surface charge versus pH relationships," *Surface science*, vol. 424, no. 1, pp. 28–35, 1999.
- [39] J. Deng, X. Lv, J. Liu, H. Zhang, K. Nie, C. Hong, J. Wang, X. Sun, J. Zhong, and S.-T. Lee, "Thin-Layer Fe_2TiO_5 on Hematite for Efficient Solar Water Oxidation," *ACS nano*, vol. 9, no. 5, pp. 5348–5356, 2015.

